Pressure-dependent large-scale seismic anisotropy induced by non-Newtonian mantle flow

John Keith K Magali, E E Ledoux, C Thomas, Yann Capdeville, Sébastien Merkel

To cite this version:

John Keith K Magali, E E Ledoux, C Thomas, Yann Capdeville, Sébastien Merkel. Pressure-dependent large-scale seismic anisotropy induced by non-Newtonian mantle flow. Geophysical Journal International, 2024, 238 (1), pp.400 - 419. 10.1093/gji/ggae165 . hal-04670847

Geophysical Journal International

Geophys. J. Int. (2024) **238,** 400–419
Advance Access publication 2024 May 11
GJI Seismology

https://doi.org/10.1093/gji/ggae165

Pressure-dependent large-scale seismic anisotropy induced by non-Newtonian mantle flow

J.K. Magali,[1,2] E.E. Ledoux,[3] C. Thomas,[2] Y. Capdeville[4] and S. Merkel[1]

[1] *Univ. Lille, CNRS, INRAE, Centrale Lille, UMR 8207 - UMET, F-59000 Lille, France. E-mail: jkvmagali@gmail.com*
[2] *Institute of Geophysics, University of Münster, Corrensstr. 24, 48149 Münster, Germany*
[3] *Department of Geology and Geophysics, University of Utah, Salt Lake City, UT 84112, USA*
[4] *Laboratoire de Planétologie et Géodynamique, CNRS, UMR 6112, Université de Nantes, 44035 Nantes Cedex 1, France*

Accepted 2024 May 5. Received 2024 March 27; in original form 2023 August 9

SUMMARY

Observations of large-scale seismic anisotropy can be used as a marker for past and current deformation in the Earth's mantle. Nonetheless, global features such as the decrease of the strength of anisotropy between ∼150 and 410 km in the upper mantle and weaker anisotropy observations in the transition zone remain ill-understood. Here, we report a proof of concept method that can help understand anisotropy observations by integrating pressure-dependent microscopic flow properties in mantle minerals particularly olivine and wadsleyite into geodynamic simulations. The model is built against a plate-driven semi-analytical corner flow solution underneath the oceanic plate in a subduction setting spanning down to 660 km depth with a non-Newtonian $n = 3$ rheology. We then compute the crystallographic preferred orientation (CPO) of olivine aggregates in the upper mantle (UM), and wadsleyite aggregates in the upper transition zone (UTZ) using a viscoplastic self-consistent (VPSC) method, with the lower transition zone (LTZ, below 520 km) assumed isotropic. Finally, we apply a tomographic filter that accounts for finite-frequency seismic data using a fast-Fourier homogenization algorithm, with the aim of providing mantle models comparable with seismic tomography observations. Our results show that anisotropy observations in the UM can be well understood by introducing gradual shifts in strain accommodation mechanism with increasing depths induced by a pressure-dependent plasticity model in olivine, in contrast with simple A-type olivine fabric that fails to reproduce the decrease in anisotropy strength observed in the UM. Across the UTZ, recent mineral physics studies highlight the strong effect of water content on both wadsleyite plastic and elastic properties. Both dry and hydrous wadsleyite models predict reasonably low anisotropy in the UTZ, in agreement with observations, with a slightly better match for the dry wadsleyite models. Our calculations show that, despite the relatively primitive geodynamic setup, models of plate-driven corner flows can be sufficient in explaining first-order observations of mantle seismic anisotropy. This requires, however, incorporating the effect of pressure on mineralogy and mineral plasticity models.

Key words: Composition and structure of the mantle; Phase transitions; Seismic anisotropy; Seismic discontinuities.

1 INTRODUCTION

Over the past four decades, seismic studies revealed the ubiquity of seismic anisotropy (i.e. directional-dependence of seismic wave velocities) across regions within the Earth's interior pertaining to boundary layers where deformation is assumed to be the largest (e.g. Montagner 1998). Most of the large-scale seismic anisotropy is observed across the upper-mantle underneath tectonic plates (e.g. Nataf *et al.* 1984; Silver 1996; Savage 1999; Boschi & Ekström 2002; Debayle & Ricard 2013; Eddy *et al.* 2022); although on some occasions, they can be detected across the Earth's crust which is often attributed to extrinsic anisotropy (Crampin 1994). Subsidiary observations are identified in the lowermost mantle across the D$''$ layer (e.g. Kendall & Silver 1998; Panning & Romanowicz 2006; Thomas *et al.* 2011; Nowacki & Nowacki 2013). At mid-mantle depths, the presence of seismic anisotropy remains enigmatic. Some studies suggest that it is nearly isotropic in the regional-scale (e.g. Kaneshima & Silver 1992; Meade *et al.* 1995; Fischer & Wiens 1996) whereas global-scale anisotropic tomography revealed a radially anisotropic mid-mantle (e.g. Panning &

Romanowicz 2006; Chang *et al.* 2015). Across the mantle transition zone (∼410–660 km), enough evidence has shown the presence of seismic anisotropy (e.g. Montagner & Kennett 1996; Visser *et al.* 2008; Panning & Romanowicz 2006; Chang *et al.* 2015; Simmons *et al.* 2019) especially around subduction zones (Wookey & Kendall 2004; Ferreira *et al.* 2019; Montagner *et al.* 2021). In this study, we take interest in the origins of seismic anisotropy in the upper mantle (UM: 100–410 km) and the upper mantle transition zone (UTZ: 410–520 km).

In terms of the *S*-wave radial anisotropy parameter ($\xi = V_{SH}^2/V_{SV}^2$) where V_{SH} and V_{SV} are both horizontally propagating but horizontally polarized and vertically polarized shear waves, respectively), there is a consensus among tomographic models of ξ that the globally averaged upper mantle (>250 km) exhibits positive *S*-wave radial anisotropy ($\xi > 1$) of about ∼5 per cent which peaks at ∼150 km and smoothly decreases to nearly 0 per cent from ∼250 km down to the 410-km seismic discontinuity (e.g. Dziewonski & Anderson 1981; Montagner & Kennett 1996; Moulik & Ekström 2014; French & Romanowicz 2014; Chang *et al.* 2015). This characteristic peak at 150 km is often attributed to deformation patterns resulting from corner-type flows across the low viscosity channel right underneath the lithosphere (Gung *et al.* 2003) whereas the rapid decline in seismic anisotropy below this depth is often interpreted in terms of a shift in the dominant deformation mechanism (Karato & Wu 1993). Alternatively, the decrease in anisotropy with depth could also be explained by a deformation restricted in the upper part of the asthenosphere such as the receding deformation induced by a relatively strong migrating overriding lithosphere (e.g. Li *et al.* 2022). Meanwhile, the average UTZ displays weak negative *S*-wave radial anisotropy ($\xi < 1$) of roughly less than 1% where most of the contribution comes from seismic anisotropy produced around subducting slabs (Montagner *et al.* 2021).

Interpreting the ubiquity of radial anisotropy in the UM and UTZ requires an understanding from where and how it originates. Large-scale seismic anisotropy mainly results from the crystallographic preferred orientation (CPO) of mantle minerals as they get progressively sheared along the convective mantle flow (Nicolas & Christensen 1987; McNamara *et al.* 2002). They are called intrinsic anisotropy since seismic anisotropy is an inherent property of the minerals themselves. Sources of seismic anisotropy that cannot be explained by CPO alone are often called extrinsic anisotropy. It refers to anisotropic signals present in seismic observations due to the effective medium averaging of preferentially oriented isotropic heterogeneities whose scales are much smaller than the wavelength of the propagating wave (e.g. Backus 1962; Wang *et al.* 2013). One such example is the radial anisotropy observed at the base of the lithosphere which has been interpreted as horizontally laminated melt that has crystallized during the thickening of the lithosphere (Auer *et al.* 2015; Debayle *et al.* 2020). Thus, extrinsic anisotropy due to small-scale structures results from the limited frequency band of seismic data.

Olivine is the most abundant anisotropic mineral in the upper mantle where it displays shear wave velocity variations of up to 18 per cent (Kumazawa & Anderson 1969). The large-scale seismic anisotropy observed in the upper mantle may result from the CPO of olivine aggregates as they get progressively sheared along the convective mantle flow. Constraints from high-pressure laboratory experiments of olivine deformation suggest the most active slip system of anhydrous olivine (type A) to be (010)[100] (Zhang & Karato 1995). For simple shear deformation, a polycrystal olivine whose elastic structure can be approximated with hexagonal symmetry (Browaeys & Chevrot 2004) may re-orient its symmetry axis to the [100] axis of olivine, and ultimately to the direction of flow. Hence, seismic anisotropy which is often parametrized in terms of a transversely isotropic (TI) medium in anisotropic imaging serves as a proxy to deduce the direction of flow in the upper mantle. The active slip systems of olivine, however, are subjected to variations in some aspects most notably water content and pressure upon which their effect on the patterns of seismic anisotropy remains to be understood (e.g. Zhang & Karato 1995; Mainprice *et al.* 2005; Raterron *et al.* 2007, 2011)

Across the UTZ, the 410-km seismic discontinuity results from the olivine to wadsleyite pressure-induced phase transformation (e.g. Katsura *et al.* 2004). Barring pyroxene which only represents 15 per cent of the volume fraction, wadsleyite is considered the most abundant anisotropic constituent of the UTZ. At ambient conditions, single crystal wadsleyite exhibits shear wave velocity variations of up to 14 per cent (Mainprice *et al.* 2000). Further down, ringwoodite and garnet are the dominant phases in the 520–660 km depth range. They, however, manifest little to no seismic anisotropy (Ringwood 1991). Because of this, it is often argued that the intrinsic seismic anisotropy observed across the UTZ mainly results from the strain-induced CPO of wadsleyite aggregates. Unlike dry olivine at low pressure, there is no definitive proxy that correlates the orientation of the flow with the preferential alignment of the crystallographic axes of wadsleyite, and the symmetry axis of its resulting polycrystal elastic tensor.

To provide an adequate explanation for the observations of seismic anisotropy, it is valuable to compare them with geodynamic predictions with constraints from mineral physics (e.g. Magali *et al.* 2021). In recent years, much work has been done to couple mantle flow models with CPO calculations for the prediction of seismic anisotropy in the upper and mid mantle in subduction or mid-ocean ridge settings (e.g. Faccenda 2014; Hedjazian *et al.* 2017; Sturgeon *et al.* 2019). Strong CPO is not predicted to form during diffusion creep. In purely viscous geodynamic simulations, strain is partitioned between diffusion and dislocation creep, and only part of the strain accommodated by dislocation creep is used to compute CPO (Karato & Wu 1993). While the aforementioned studies practised strain partitioning, simpler models where all deformation is accommodated by dislocation creep still predicted the observed distribution of large-scale anisotropy provided that the deformation is confined in the shallow part of the subplate mantle (Faccenda & Capitanio 2012, 2013). These geodynamic simulations, however, ignored the pressure-dependence of olivine textures which could be a potentially viable explanation for the decrease of the observed radial anisotropy parameter ξ between 250 and 410 km (Mainprice *et al.* 2005).

In this study, we investigate the effect of pressure on the observed large-scale radial anisotropy in the upper mantle and the upper part of the transition zone by implementing pressure-induced slip transitions and the most recent dislocation slip data of wadsleyite in CPO computations. We test this method for a non-Newtonian corner flow model of the entrained mantle underneath the oceanic plate and of the subslab mantle. We then apply a tomographic filtering technique, called elastic homogenization, based on the minimum wavelength considered in seismic tomography (Capdeville *et al.* 2015; Magali *et al.* 2021). The output is a smooth model of radial anisotropy that is compatible with seismic tomography assuming perfect data coverage (Capdeville & Métivier 2018). This work is not intended to completely unravel the origin of large-scale seismic anisotropy in the mantle by exploring variations in some parameters that would change its pattern such as plate speeds and the subduction angle. Rather, we showcase a method that adds pressure-induced slip transitions of anisotropic minerals in geodynamic modelling, and establish that pressure effects on plastic deformation in these minerals are visible even in the tomographic version of the mantle.

2 BACKGROUND: ELASTIC HOMOGENIZATION

Elastic homogenization refers to a class of methods that aims to average the fine-scale properties of an elastic medium possessing small-scale spatial heterogeneities and retrieve their large-scale expression using a set of highly non-linear upscaling relations (e.g. Backus 1962; Hashin & Shtrikman 1963; Sánchez-Palencia 1980; Allaire 1992; Capdeville *et al.* 2010; Guillot *et al.* 2010). In wave propagation theory, homogenization removes spatial heterogeneities in density ρ and in the elastic tensor $\mathbf{c}$ of a medium whose scales are smaller than the minimum wavelength $\lambda_{\min}$ of the observed seismic wavefield, and instead replace them with the effective properties ρ^* and $\mathbf{c}^*$. In this way, standard wave equation solvers operate on a medium containing ρ^* and $\mathbf{c}^*$, and, in theory, yield displacements similar to the fine-scale medium sampled by $\lambda_{\min}$ up to a certain error limit. For 1-D stratified media, Backus (1962) derived analytical upscaling relations where a vertically transverse isotropic (VTI) medium is the long-wavelength equivalent of a horizontally layered isotropic medium (Fig. 1a). Homogenization techniques have also been developed for stochastic (Blanc *et al.* 2007; Bensoussan *et al.* 2011) and non-layered media (McLaughlin 1977; Hornby *et al.* 1994) among others.

The true Earth, however, is a non-periodic and multiscale medium. This motivated Capdeville *et al.* (2015) to develop a fast-Fourier homogenization (FFH) algorithm for a 3-D fine-scale elastic medium with no natural scale separation. The iterative algorithm is heavily based on the extensive usage of fast Fourier transforms to solve the periodic Lippman–Schwinger equation (Moulinec & Suquet 1998). The output is a simple mesh-less upscaled elastic medium (i.e. the effective elastic properties). The method initially served as a pre-processing step to compute synthetic seismograms in a fast and efficient manner. It has been applied in recent years to quantify extrinsic anisotropy due to small-scale isotropic heterogeneities (Alder *et al.* 2017). For instance, Alder *et al.* (2017) demonstrated that in a 2-D mechanically mixed isotropic mantle, horizontal laminations produce positive radial anisotropy ($\xi > 1$) whereas vertical laminations produce negative radial anisotropy ($\xi < 1$) (Fig. 1b). It has also been applied to estimate the contribution of structural layering and CPO to the effective radial anisotropy in a tomographic image of the upper mantle underneath oceanic plates (Magali *et al.* 2021). It was also used for downscaling to recover fine-scale properties from a synthetic tomographic model inferred from a full waveform inversion (Hedjazian *et al.* 2021).

Seismic tomography poses two main difficulties that hinder the recovery of the true elastic medium: (i) uneven distribution of ray path coverage and (ii) limited frequency band of seismic data. In practice, (i) can be be accounted for by operating the resolution matrix $\mathcal{R}$ constructed from a global tomographic model (Simmons *et al.* 2019) onto our models of seismic anisotropy derived from geodynamic and CPO evolution calculations. For simplicity, we ignore the effect of limited data coverage in this study. By considering (ii), Capdeville & Métivier (2018) verified numerically that a tomographic model obtained from a full-waveform inversion converges towards the effective elastic medium recovered from the FFH algorithm at spatial wavelengths longer than λ_0. The upscaling relations built from the FFH algorithm can be viewed as a first-order tomographic operator $\mathcal{H}$ that when applied to the true elastic medium $\mathbf{c}$, yields the effective elastic medium $\mathbf{c}^*$:

$$\mathbf{c}^* = \mathcal{H}(\mathbf{c}) \tag{1}$$

Hence, we can treat $\mathbf{c}^*$ as the best possible image one could obtain from seismic tomography assuming perfect data coverage. Following the work of Magali *et al.* (2021), we apply this ‘tomographic operator’ hypothesis to filter our predicted models of strain-induced seismic anisotropy. The result is a smooth version, one that is comparable to a seismic tomography model

3 METHODS

3.1 Corner flow representation of plate-driven mantle flow

Corner flow solutions, albeit rudimentary, offer a fast and efficient way to compute velocity fields that mimic the general patterns of plate-driven motion. Assuming incompressibility and neglecting inertial and buoyancy forces, we begin by seeking a semi-analytical solution of subslab flow to the conservation of mass and momentum equation for viscous fluid flow (Tovish *et al.* 1978; Batchelor 2000):

$$\begin{aligned} &\nabla \cdot \mathbf{u} = 0, \\ &\nabla p - \nabla \cdot 2\eta \cdot \dot{\varepsilon}(\mathbf{u}) = 0, \end{aligned} \tag{2}$$

where $\mathbf{u}$ is velocity, p is total pressure, $\dot{\varepsilon}$ is strain rate and η is effective viscosity whose form follows a strain rate-dependent rheology given by (Ribe 1989):

$$\eta = \eta_0 \left[\frac{\dot{\varepsilon}_{\mathrm{II}}}{\dot{\varepsilon}_0} \right]^{\frac{1-n}{n}}, \tag{3}$$

with η_0 being the reference viscosity, $\dot{\varepsilon}_{\mathrm{II}}$ the second invariant of the strain rate tensor and n the power-law index. Our corner flow model does not take into account the pressure and temperature dependence of viscosity. Although an $n \approx 3.5$ is suggested to properly model deformation by dislocation creep of olivine (e.g. Hirth & Kohlstedt 2003), here we select $n = 3$ to obtain analytical non-Newtonian corner flow solutions that is representative of passive mantle flows (Tovish *et al.* 1978; Hedjazian & Kaminski 2014). In-plane polar coordinates $[r, \theta]$, the solution to eq. (2) is given by the analytical stream function $f(r, \theta) = r\Theta(\theta)$ (Batchelor 2000), where Θ is a transcendental equation whose form depends on the stress exponent (Tovish *et al.* 1978). For $n = 3$, this gives (Hedjazian & Kaminski 2014):

$$\Theta(\theta) = a_1 \sin\theta + a_2 \cos\theta + a_3 \Pi(\theta, a_4), \tag{4}$$

with:

$$\Pi(\theta, a_4) = 27 \cos\frac{\sqrt{5}}{3}(\theta + a_4) - \cos\sqrt{5}(\theta + a_4), \tag{5}$$

where a_{1-4} are constant coefficients that are determined numerically from the mechanical boundary conditions imposed (Tovish *et al.* 1978). For subslab flow, Fig. 2(a) shows the boundary conditions as well as some streamlines traced by the flow. Here, we choose a subduction angle of $\theta = 45^\circ$ and a plate velocity of $v_r = 1\ \mathrm{cm\,yr^{-1}}$. Such values may represent a slow-moving oceanic lithosphere where we expect penetration at the 660-km seismic discontinuity due to the negative trade-off between slab buoyancy and backward trench migration speed (Christensen 1996).

Mantle aggregates subjected to a macroscopic velocity gradient along flow streamlines experience progressive deformation leading

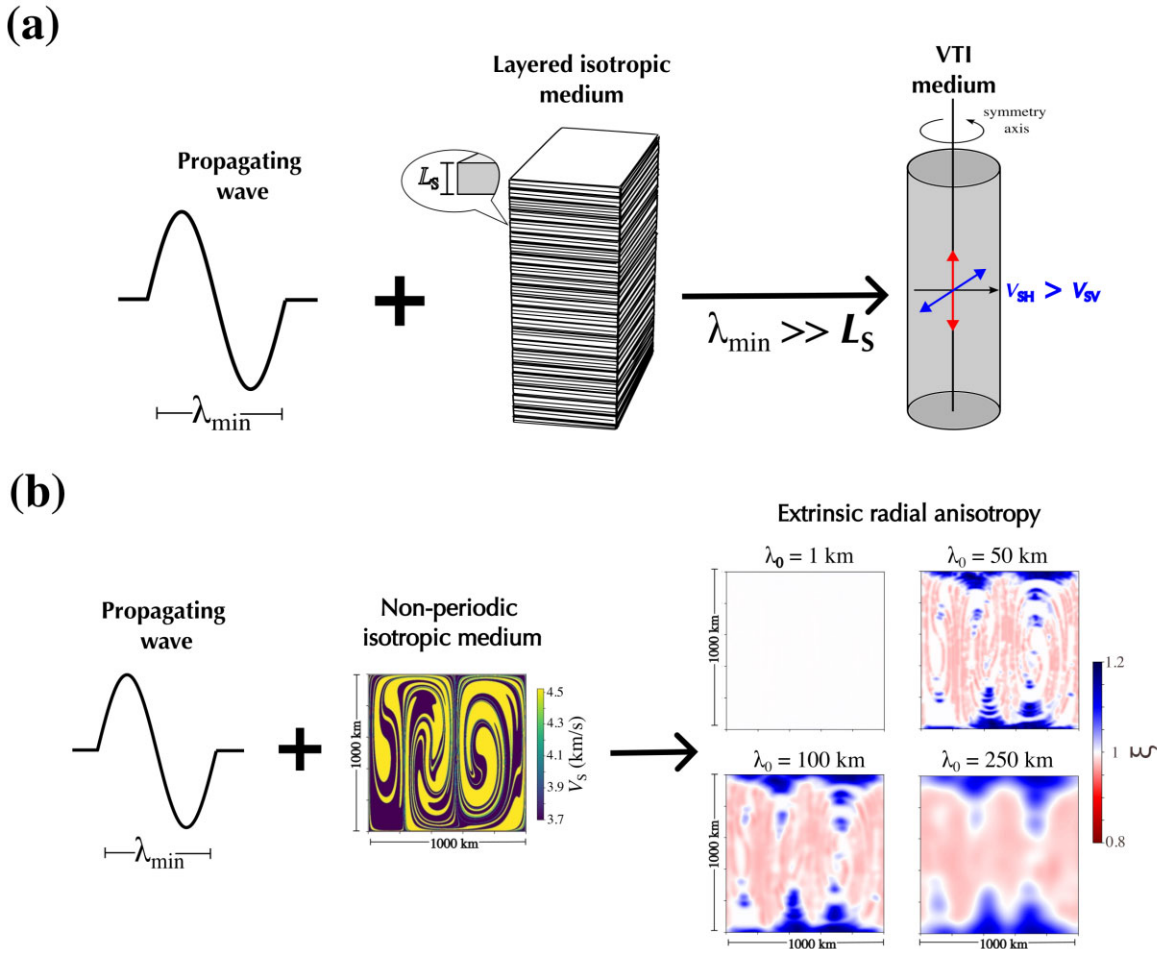

Figure 1. Extrinsic anisotropy is induced under two conditions: (i) when the wavelength of the propagating wave $\lambda_{\min}$ is much larger than the scale of the heterogeneities L_S and (ii) when the contrast in elastic moduli is sufficiently large. (a) Schematic diagram depicting Backus' homogenization (Backus 1962). A horizontal-layered isotropic medium is 'seen' as a vertically transverse isotropic medium (VTI) with $V_{SH} > V_{SV}$ (and hence $\xi > 1$) for $\lambda_0 > > L_S$. (b) Extrinsic radial anisotropy produced from a 2-D non-periodic isotropic medium for several λ_0 using the fast-Fourier homogenization algorithm of Capdeville *et al.* (2015). Stretching and thinning due to convection generate horizontal and vertical fine laminations with $\xi > 1$ and $\xi < 1$, respectively. This 2-D medium can be regarded as an amalgamation of Backus' layers with two distinctive orientations: vertical and horizontal layering. λ_0 shorter than the scale of laminations (e.g. $\lambda_0 = 1$ km) does not generate any extrinsic anisotropy.

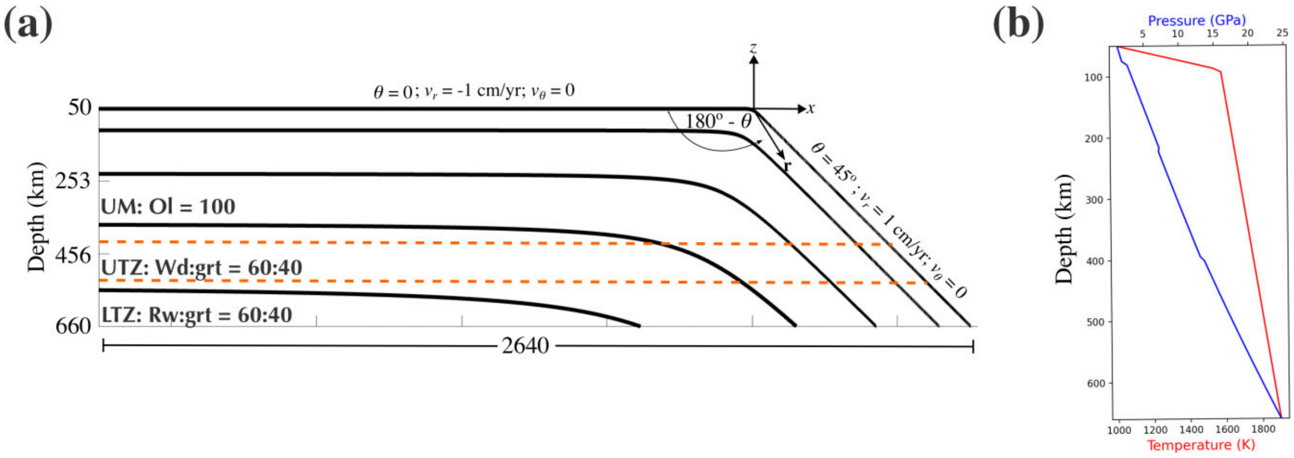

Figure 2. (a) Corner flow representation of subslab mantle flow. Boundary conditions include a subduction angle of $\theta = 45°$ and a plate velocity of $v_r = 1$ cm yr^{-1}. Solid black lines are some streamlines traced by the flow. Dashed orange lines indicate the 410 and 520 km phase transition boundaries. For depths $z < 410$ km (upper mantle), anisotropy development is dictated by the plastic deformation of olivine aggregates. For $410 \leq z \leq 520$ km (UTZ), anisotropy development is governed by wadsleyite. Below 520 km, the LTZ is assumed isotropic. Modal abundancies in the transition zone replicate a pyrolitic mantle composition. (b) Pressure and temperature profiles included in our synthetic mantle models for olivine CRSS and single crystal elastic moduli calculations.

to CPO development. In the case of mantle corner flows, there exists an analytical macroscopic velocity gradient tensor L. In polar coordinates, it simply corresponds to a simple shear about the $\hat{\theta}$ direction in the $[r, \theta]$ plane (Hedjazian & Kaminski 2014):

$$L_{r\theta} = \frac{\Theta(\theta) + \Theta''(\theta)}{r} \begin{pmatrix} 0 & 1 \\ 0 & 0 \end{pmatrix} \tag{6}$$

where Θ'' denotes the second derivative in θ.

3.2 Calculating strain-induced seismic anisotropy

3.2.1 Modelling texture evolution

To model texture evolution, we first trace streamlines using a fourth-order Runge–Kutta integration scheme and then compute local velocity gradients via eq. (6) at each discrete step along the streamline. Polycrystal aggregates are then assigned at the initial time step. Each aggregate is composed of 3000 grains with initial non-random CPO that were computed from a mantle corner flow model underneath a mid-ocean ridge. The governing and constitutive equations for this model are identical to eqs (2) and (3), and the boundary conditions and the solution for $n = 3$ is listed in Hedjazian & Kaminski (2014). The modal abundancies are as follows: UM ($z < 410$ km): 60 per cent olivine and 40 per cent pyroxene, UTZ ($410 \leq z \leq 520$ km): 60 per cent wadsleyite and 40 per cent garnet, and lower transition zone (LTZ) ($520 < z \leq 660$ km): 60 per cent ringwoodite and 40 per cent garnet (Fig. 2a). From their initial positions (i.e. the first time step), we allow strain evolution in the aggregates forward in time along the streamlines traced earlier using a method to be discussed in the succeeding section. We then set an arbitrary boundary at 410 and 520 km corresponding to the phase transition boundary between olivine and wadsleyite, and wadsleyite and ringwoodite, respectively. Each time an aggregate crosses such boundaries, the crystallographic orientations are randomized to mimic the erasure of textures when a material crosses a phase transition boundary, as demonstrated by experiments in Smyth *et al.* (2012) and Ledoux *et al.* (2023). Upon erasure at 410 km, strain evolution is re-initialized, whereas at 520 km, the random orientations are retained to simulate an isotropic LTZ. Note that we also consider the garnet phase in the UTZ to be isotropic due to its isotropic elasticity and plasticity behaviour (Pamato *et al.* 2016; Girard *et al.* 2020; Vennari *et al.* 2021). Similarly, we model the pyroxene phase in the UM as isotropic due to our limited understanding of its rheological properties (e.g. Hansen *et al.* 2021).

To compute the strain-induced anisotropy of a given mineral aggregate, we use the viscoplastic self-consistent (VPSC) method (Molinari *et al.* 1987; Lebensohn & Tomé 1993). It uses an 'average field' formalism where individual grains are treated as an ellipsoidal inclusion making up the polycrystalline aggregate. The core of the algorithm is finding an Eshelby solution to the self-consistent equations by routinely computing the macroscopic stress Σ_{kl}, single crystal strain rate $\dot{e}_{ij}$, and the viscoplastic compliance tensor $\tilde{M}_{ijkl}$ (i.e. a tensor that depends on the rheology of the aggregate and the shape of the grain) at each time step:

$$-\alpha \tilde{M}_{ijkl}(\sigma_{kl} - \Sigma_{kl}) = \dot{e}_{ij} - \dot{\varepsilon}_{ij}. \tag{7}$$

Here, $\dot{\varepsilon}_{ij}$ is an input which refers to the symmetric part of the macroscopic velocity gradient tensor (i.e. macroscopic strain rate) computed from eq. (6) for each step along the streamline. Other inputs include the slip and twinning systems s and the corresponding critically resolved shear stresses (CRSS) τ_0^s that control the deformation response of a single crystal due to the grain-scale stress σ_{kl}, and the parameter α which regulates grain interaction. We choose $\alpha = 1$ after the tangent model which provides a sufficient representation of the viscoplastic behaviour of polycrystalline aggregates (Lebensohn & Tomé 1993). Once the macroscopic states $(\boldsymbol{\Sigma}, \dot{\boldsymbol{\varepsilon}})$ conform with the average of the microscopic states $(\boldsymbol{\sigma}, \dot{\boldsymbol{e}})$ in the effective aggregate to a certain tolerance level which we set to 0.001 by default, the code outputs the textures in terms of three Euler angles that describe the orientation of each crystal making up the aggregate at each step along the streamline. In this work, CPO computation is terminated once strains accrued for roughly 10 Myr.

3.2.2 Pressure-induced slip transitions of olivine

Traditional practices of joint geodynamic and texture evolution modelling involve the implementation of a single set of olivine slip systems to study strain-induced seismic anisotropy in the upper mantle using a kinematic approach (e.g. Faccenda & Capitanio 2013; MacDougall *et al.* 2017; Hedjazian *et al.* 2017; Sturgeon *et al.* 2019; Fraters & Billen 2021, to name a few) or the average field kind (e.g. Li *et al.* 2014). It is, however, observed experimentally that olivine displays plastic behaviour that will depend on pressure and hence depth in the Earth's mantle (e.g. Couvy *et al.* 2004; Raterron *et al.* 2007; Jung *et al.* 2009; Ohuchi *et al.* 2011) which may explain the decrease of seismic anisotropy commencing at ∼200 km observed in seismic tomography models (e.g. Simmons *et al.* 2019).

Dominant slip systems of olivine given by [100](010) and [001](010) have shown to be promoted individually by compression and simple shear experiments. Under low pressure conditions, Raterron *et al.* (2012) reported that the coupled activities of [100](001) and [001](100) complement the [100](010) slip system, yielding a substantial amount of seismic anisotropy akin to those that are observed across the low viscosity channel underneath oceanic ridges. At larger pressures comparable to ∼250-km depth and below, the [001](010) slip system is favoured yielding much lower levels of seismic anisotropy. Tielke *et al.* (2016) performed direct simple shear experiments to measure individually the [100](001) and [001](100) slip systems. They later revealed that under lithospheric mantle conditions, [100](001) exhibits larger activity than [001](100). Under asthenospheric conditions, [001](100)]gradually takes over with increasing depths. To our knowledge, individual activations of the [100](021) and [001]{110} slip systems were never observed experimentally to this date. Pressure dependence of their CRSS are estimated via a numerical framework based on *ab initio* density functional theory (Durinck *et al.* 2007). Raterron *et al.* (2014) then used these experimental flow laws and theoretical estimates to lay the groundwork of predicting the CRSS of olivine slip systems representing a 20 My oceanic geotherm at a strain rate of $\sim 10^{-15}$ s^{-1} (refer to table 1 of Raterron *et al.* 2014).

To include pressure-induced slip transitions in olivine, we first interpolate density ρ inferred from PREM (Dziewonski & Anderson 1981) with depth z and then compute the hydrostatic pressure to add depth profiles of pressure in our corner flow models (Fig. 2b). We then fit second-order polynomial functions to the CRSS reported by Raterron *et al.* (2014) with P. Coefficients are tabulated in Table 1. Afterwards, we integrate these functions into VPSC so that a new CRSS is initialized each time strain accumulates along the streamline traced by the aggregate. Finally, we establish the relationship between the local shear rate $\dot{\gamma}$ in a slip system s of a given crystal at the current step along the streamline with pressure through the

Table 1. Coefficients of the second-order polynomials that fit the critically resolved shear stress (CRSS) τ_0 as a function of pressure P for a given slip system of olivine reported in Raterron *et al.* (2014). The function takes the form $\tau_0(P)_{\langle uvw\rangle\{hkl\}} = \omega_1 P^2 + \omega_2 P + \omega_3$ where $\langle uvw\rangle\{hkl\}$ denotes a given slip system. Note the CRSS values in this table are relative as VPSC calculations are only sensitive to relative and not absolute values.

	[100](010)	[001](010)	[001](100)	[100](001)	[100]{021}	[001]{110}
ω_1	0.0026	0.0006	0.0017	0.002	0.0026	0.0017
ω_2	-0.018	-0.022	0.001	0.0014	-0.018	-0.066
ω_2	0.188	0.34	0.152	0.184	0.188	1.02

CRSS $\tau_0^s(P)$:

$$\dot{\gamma}^s = \dot{\gamma}_0 \left[\frac{\tau_r^s}{\tau_0^s(P)}\right]^{n^s} \tag{8}$$

where $\dot{\gamma}_0$ is the reference shear rate, n^s is the stress exponent of the slip system, and τ_r^s its resolved shear stress. For a given system s, τ_r refers to the component of the applied stress that causes dislocation slip whereas τ_0 is simply the minimum amount of stress required to initiate it. The sum of $\dot{\gamma}$ over all possible slip systems s is the strain rate $\dot{e}_{ij}$ of the grain appearing in eq. (7). Although our functions only depend on pressure, the CRSS of olivine reported by Raterron *et al.* (2014) also varies with temperature that is typical to a 20 Myr oceanic geotherm. Under this circumstance, computing seismic anisotropy might lead to poor predictions in regions that are not representative of such a temperature profile. Because of this, we set an arbitrary temperature gradient starting from a surface adiabatic temperature of 293 K up to 1580 K corresponding to the base of the lithosphere (z = 90 km), and another linear gradient from 1580 K at z = 90 km up to 1900 K at z = 660 km to match the temperature profile found in Raterron *et al.* (2014) (Fig. 2b). These temperature and pressure profiles are used to introduce $P-T$ dependence of the elastic moduli.

Olivine lacks four independent slip systems and hence may fail to accommodate an arbitrarily imposed macroscopic deformation. To remedy this, we adopt the procedure of Tommasi *et al.* (2000) by including some fictitious slip systems: <110 > {111} and <111 > {110} which replicates an isotropic relaxation mechanism. Castelnau *et al.* (2008) showed these fake slip systems provide a negligible contribution to the overall strain, however, they are necessary to simulate the texture evolution of olivine unless a more realistic relaxation mechanism is implemented such as those found in the second-order VPSC method. In essence, fictitious slip systems or isotropic relaxation mechanisms tend to reduce the strength of texture, and hence seismic anisotropy, without modifying its main features (e.g. orientation distribution, direction of fast wave propagation, etc., Castelnau *et al.* 2010).

In this work, we consider two cases: (i) an upper mantle consisting of an A-type olivine where we adopt the slip systems of Tommasi *et al.* (2000) and (ii) an upper mantle with P-dependent olivine textures. We then compare the resulting strain-induced seismic anisotropy before and after the application of homogenization. Table 2 lists the active slip systems and the corresponding CRSS of A-type olivine and the P-dependent scenario at selected pressures relevant to the upper mantle.

3.2.3 Slip mechanisms in wadsleyite

We perform similar VPSC simulations to model the evolution of microstructures of wadsleyite. Reports of dominant slip systems and microstructural types have been inconsistent in the literature, some arguing for microstructures controlled by ⟨111⟩{101} and [100](0kl) (Thurel & Cordier 2003; Tommasi *et al.* 2004; Ritterbex *et al.* 2020), [001](010) (Kawazoe *et al.* 2013), a combination of ⟨111⟩{101}, [100](0kl), and [001](010) (Demouchy *et al.* 2011), with an effect of water content and temperature (Ohuchi *et al.* 2014). Recently, (Ledoux *et al.* 2023) proposed a combined and comprehensive analysis of wadsleyite microstructures, based on new *in situ* high-pressure high-temperature multigrain crystallography experiments and results from the literature. Wadsleyite microstructures are sorted into a set of five temperature and water-dependent types. Most notably, model B_{wd}-type, with dominant slip on ⟨111⟩{101}, [100]{0kl}, [001](010) in which [001](010) controls the microstructure is found to dominate in somewhat dry regions of the mantle transition zone, model A_{wd}-type with dominant slip on ⟨111⟩{101} and [100]{0kl} prevails in cold regions such as subducting slabs, and model C_{wd}-type, dominant slip on ⟨111⟩{101} and [001](010) applies to regions with high water content (greater than 600 wt ppm). This paper focuses on average properties of the mantle transition zone and, thus, on streamlines outside of subduction zones. For this, we choose B_{wd}-type and C_{wd}-type wadsleyite, for modelling a dry and a wet transition zone, respectively. The active slip systems and their respective CRSS are tabulated in Table 2.

3.2.4 Elastic constants and quantifying seismic anisotropy

Once textures are calculated, we apply a Voigt–Reuss–Hill averaging scheme with respect to a P- and T-dependent single crystal elastic constant $\mathbf{c}_0$ according to the orientation and the volume fraction of the grains to get a local polycrystalline elastic tensor $\mathbf{c}(P, T)$ (Mainprice 1990). Here, the P- and T-dependence of $\mathbf{c}_0$ are estimated using corrections to $\mathbf{c}_0$ at ambient conditions. These corrections are often characterized in terms of first-order partial derivatives of $\mathbf{c}$ with T and up to second-order with P to include the non-linear dependence of $\mathbf{c}_0$ with P at high pressures. In practice, the elastic constants are measured experimentally through Brillouin spectroscopy or theoretically through first-principles calculations.

We take the single crystal elastic constants of olivine from Mao *et al.* (2015) where they measured the elastic constants up to 900 K and 20 GPa using Brillouin spectroscopy in an externally heated diamond anvil cell. We then extrapolate the values to $T > 900$ K by estimating the first-order T derivative and then interpolate in the given pressure range by computing P derivatives up to the second order. Meanwhile, those of ringwoodite and garnet are retrieved from Sinogeikin *et al.* (2003), Chai *et al.* (1997) and Sinogeikin & Bass (2002) which are summarized in Table 3 of Faccenda (2014).

The combined pressure–temperature dependence of the single crystal elastic constants of wadsleyite are not as widely constrained

Table 2. Active slip systems and their corresponding CRSS of: (a) P-dependent olivine, (b) A-type olivine (i.e. dry and low pressure), (c) B_{wd}-type wadsleyite (i.e. dry), and d) C_{wd}-type wadsleyite (i.e. hydrous).

Slip system	P-dependent olivine[a]			A-type olivine[b]	B_{wd}-type wadsleyite[c]	C_{wd}-type wadsleyite[d]
	Pressure (GPa)*					
	3.45	7.9	13.3			
[100](010)	0.15	0.21	0.42	0.1	1	10
[001](010)	0.27	0.2	0.15	0.2	0.1	1
[001](100)	0.17	0.26	0.46	0.3	–	–
[100](001)	0.21	0.32	0.56	0.1	1	10
[001]{110}	0.8	0.61	0.45	0.6	–	–
[100]{011}	–	–	–	0.4	1	10
[100]{031}	–	–	–	0.4	–	–
[100]{021}	0.15	0.21	0.42	–	1	10
<111 > {101}	–	–	–	–	0.5	0.5
<111 > {110} + <110 > {110}†	1	1	1	1	–	–

* The pressure values shown here are representative of depths: ∼100 km, 240 km, 405 km, and temperatures: ∼1600 K, 1670 K, 1760 K.

† Fictitious slip systems to accommodate crystal rotations in olivine.

Table 3. P–T derivatives of dry and wet (1.63 wt. per cent H_2O) Fe-bearing wadsleyite single crystal elastic constants estimated from a simple polynomial fit with reference values set at $T_0 = 300$ K and $P_0 = 0$ GPa.

Wadsleyite	P–T derivatives	Units	c_{11}	c_{22}	c_{33}	c_{44}	c_{55}	c_{66}	c_{12}	c_{13}	c_{23}
Dry	$\partial c_{ij}/\partial T$	$\mathrm{GPa \cdot K^{-1}}$	−0.036	−0.041	−0.034	−0.014	−0.013	−0.012	−0.008	−0.009	−0.011
	$\partial c_{ij}/\partial P$	–	7.12	7.6	7.2	1.45	1.51	1.3	3.26	3.25	3.95
	$\partial^2 c_{ij}/\partial P^2$	$\mathrm{GPa^{-2}}$	−0.09	−0.1	−0.11	−0.035	−0.028	−0.029	0	0	−0.085
Wet	$\partial c_{ij}/\partial T$	$\mathrm{GPa \cdot K^{-1}}$	−0.029	−0.03	−0.037	−0.017	−0.011	−0.014	−0.005	−0.008	−0.012
	$\partial c_{ij}/\partial P$	–	7.48	5.66	8.8	0.91	0.86	2.37	3.68	2.36	3.7
	$\partial^2 c_{ij}/\partial P^2$	$\mathrm{GPa^{-2}}$	−0.18	0	−0.19	0	0	−0.034	0	0	0

as those of olivine, nor the effect of Fe and water content. In fact, Kawazoe *et al.* (2013) used 300 K elastic constants for estimating anisotropy and Saki *et al.* (2018) built an isotropic composite model based on data for olivine. Núñez-Valdez *et al.* (2013) evaluated the elastic moduli and their P–T dependence for dry Mg_2SiO_4 wadsleyite using first-principles calculations. More recently, Zhou *et al.* (2022) measured the single crystal elastic constants of hydrous Fe-bearing wadsleyite (Fe# = 9.4(2), 0.15(4) wt.% H_2O) up to 700 K and 20 GPa using Brillouin scattering, which can be compared with the results of Wang *et al.* (2019) who performed computations for 1.63 wt per cent H_2O-bearing wadsleyite. Ledoux *et al.* (2023) showed the computed seismic anisotropy in a wadsleyite polycrystal using the elastic constants of Zhou *et al.* (2022) is consistent with that of Wang *et al.* (2019). From these studies, it appears that the large-scale seismic anisotropy in the UTZ is strongly affected by water. It may hence be imperative to build two models of elastic properties, one against the calculations of Núñez-Valdez *et al.* (2013), relevant for a dry mantle transition zone, and one against the measurements of Zhou *et al.* (2022), relevant for a hydrous mantle transition zone. Fig. 3 summarizes these two sets of elastic moduli with P and T in the following ranges P: 0−25 GPa and T: 1600−1800 K, and Table 3 lists the P–T derivatives estimated from a simple polynomial fit.

Numerous seismic tomography studies parametrize seismic anisotropy in terms of the S-wave radial anisotropy parameter ξ. It quantifies the relative speed of a horizontally propagating, horizontally polarized S wave (V_{SH}) versus a horizontally propagating, vertically polarized S wave (V_{SV}). Given our elastic tensor $\mathbf{c}$ in Voigt notation, we can compute ξ by first expressing V_{SH} and V_{SV} in terms of linear combinations of $\mathbf{c}$. By decomposing $\mathbf{c}$ into an azimuthally averaged vertically transverse isotropic (VTI) medium, we have (Montagner & Nataf 1986):

$$V_{SH}^2 = \frac{1}{2\rho}\left(\frac{1}{4}(c_{11} + c_{22}) - \frac{1}{2}c_{12} + c_{66}\right),$$
$$V_{SV}^2 = \frac{1}{2\rho}(c_{44} + c_{55}), \qquad (9)$$

and ξ is henceforth:

$$\xi = \frac{V_{SH}^2}{V_{SV}^2}. \qquad (10)$$

From this point forward, radial anisotropy pertains to the parameter ξ.

3.3 Homogenization of the mantle model

The fast-Fourier homogenization (FFH) algorithm works under the assumption that the observed wavefield sampling the true elastic medium contains a minimum wavelength $\lambda_{\min}$ designated to a maximum frequency $f_{\max}$ and the slowest S-wave velocity $V_{S,\min}$ (Capdeville & Marigo 2007; Capdeville *et al.* 2010; Guillot *et al.* 2010). Instead of $\lambda_{\min}$ however, the algorithm inputs user-defined parameters λ_0 and ε_0 called homogenization wavelength and scale-separation parameter, respectively, with $\lambda_{\min} = \lambda_0/\varepsilon_0$. These parameters are described in complete detail in Capdeville *et al.* (2010, 2015). Using the tomographic operator hypothesis of Guillot *et al.* (2010); Capdeville *et al.* (2015), we can invoke eq. (1) to the spatial distribution of elastic tensors $\mathbf{c}$ making up the mantle model. We then obtain an effective elastic medium $\mathbf{c}^*$ that is smooth and devoid of small-scale heterogeneities up to the homogenization wavelength

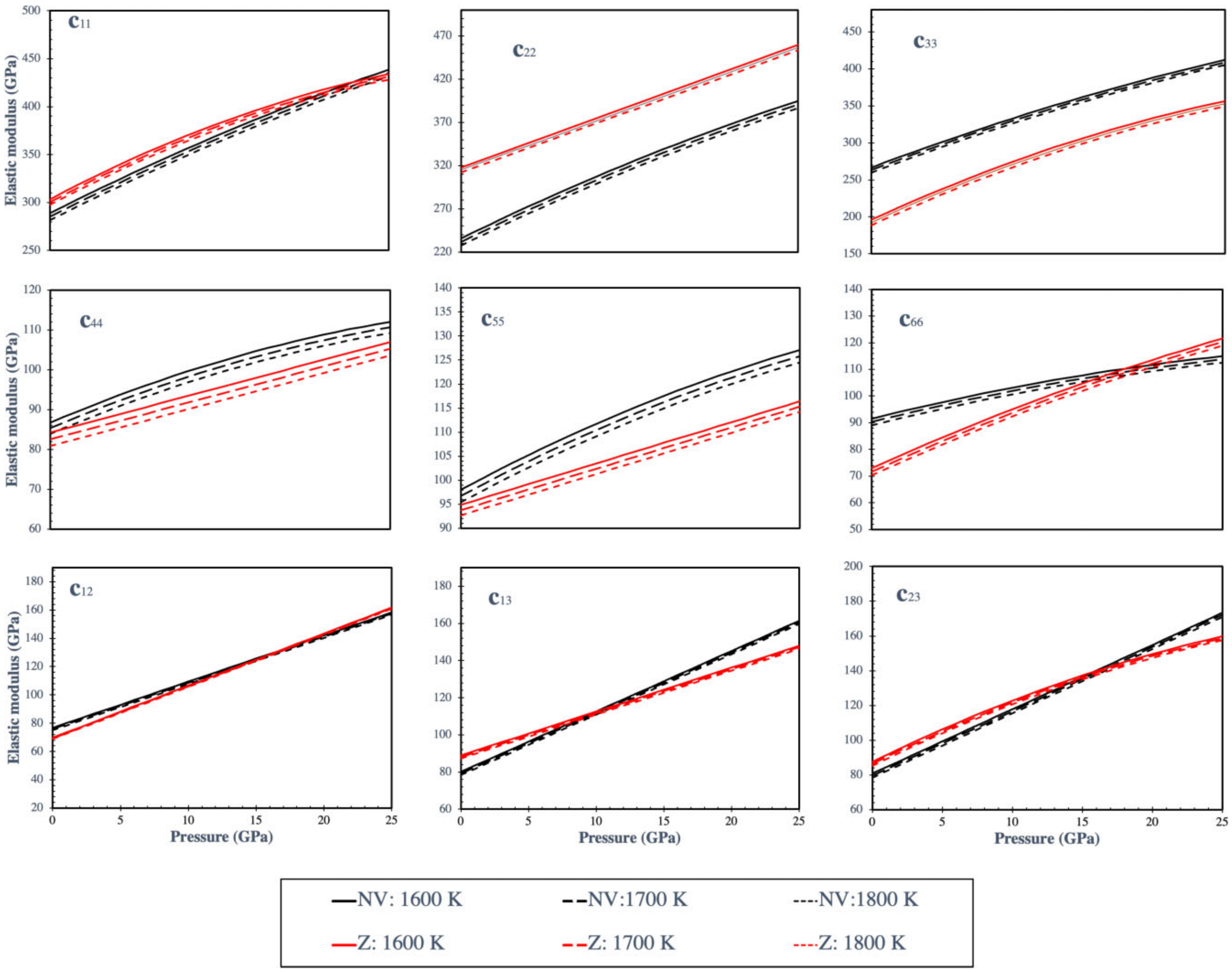

Figure 3. Pressure and temperature dependence of the single crystal elastic constants of dry wadsleyite (Núñez-Valdez *et al.* 2011, 2013, in black) and hydrous wadsleyite (Zhou *et al.* 2022, in red).

λ_0. This effective medium is then compatible, to first order, with tomographic models recovered from a full waveform inversion assuming perfect data coverage (Capdeville & Métivier 2018; Magali *et al.* 2021). After obtaining $\mathbf{c}^*$, the effective radial anisotropy (i.e. the homogenized counterpart of ξ) can be computed through eqs (9) and (10) accordingly. In this work, we fix the scale separation parameter to $\varepsilon_0 = 0.5$, and set the homogenization wavelength to $\lambda_0 = 100$ km.

4 RESULTS

The rheology of olivine aggregates are a function of some key parameters such as grain size, pressure P, temperature T and water content (Hirth & Kohlstedt 2003). Empirical rheological laws can be established that when extrapolated to upper mantle conditions, they display a composite diffusion-dislocation creep as a deformation mechanism. Karato & Wu (1993) showed that intracrystalline plasticity by dislocation creep promotes the development of CPO, whereas isotropic mechanisms related to diffusion creep do not produce any CPO. Thus, the weakening of seismic anisotropy with depth observed in tomographic models of the upper mantle is often associated with the shift in the dominant deformation mechanism (i.e. from dislocation to diffusion creep). For this reason, rheological parameters used in mantle flow models are often fine-tuned to match seismological observations (e.g. Boneh *et al.* 2015; Hedjazian *et al.* 2017). As previously mentioned, the standard approach to do this is to scale the macroscopic velocity gradient tensor by the fraction of the effective viscosity accommodated by dislocation creep, and then compute the CPO for a single type of olivine fabric. However, the weakening of seismic anisotropy with depth can also be explained by the pressure-dependence of olivine plasticity (Mainprice *et al.* 2005; Raterron *et al.* 2007; Ohuchi *et al.* 2011; Raterron *et al.* 2011; Jung *et al.* 2009) which can be implemented numerically by formulating the CRSS as a function of pressure (Raterron *et al.* 2014). When accounted in geodynamic flow simulations, this presents a CPO model whose dislocation slip activities vary with pressure, and hence a dynamic representation of mantle fabric transitions.

Before we test this hypothesis, one must first consider that the deformation patterns are well-distributed and extend down to the base of the upper mantle. In this way, the pressure-dependent mechanism remains an active process throughout the modelling domain. We estimate the amount of strain accumulated across the subplate and subslab mantle by calculating the natural strain E_0 through the formula:

$$E_0 = \frac{1}{2}\ln(\zeta_1/\zeta_2), \tag{11}$$

where ζ_1 and ζ_2 are the long and short axes, respectively, of the finite strain ellipse (FSE). Fig. 4(a) illustrates how the second invariant of the strain rate tensor $\dot{\varepsilon}_{\mathrm{II}}$ is localized close to the trench which resulted from changes in flow direction at the trench. The strength of $\dot{\varepsilon}_{\mathrm{II}}$ spreads and aggressively fades with depth across the subslab mantle while it is minimal across the subplate mantle which could be explained by small velocity gradients stemming from the imposition of plate-driven motion. To better characterize the current state of deformation in our mantle model, we calculate the amount of strain accrued for 10 My through the natural strain E_0 (Fig. 4b). The FSE of the tracers were already initially deformed as they entered the current modelling domain (i.e. subplate and subslab mantles). Once the tracers entered the domain, the small velocity gradients within the subplate mantle provided a small contribution to the deformation of the FSE. Because of this, the deformation patterns predicted from the ridge model are preserved across the subplate mantle. Relatively large natural strains stretching down to the deep upper mantle (i.e.∼300–410 km) can be observed in Fig. 4(b), which are enough to generate strain-induced seismic anisotropy down to these depths (Ribe 1992).

We now compare the CPO and the resulting seismic anisotropy from the standard approach of using a single olivine fabric type (in this case an A-type fabric) and from the *P*-induced olivine dislocation slip transitions. Fig. 5 (middle panels) illustrates the effect of pressure-induced slip transitions to the CPO of an olivine polycrystal as it becomes progressively sheared along a streamline (path 1). Along the same streamline, the standard approach using A-type olivine is also displayed in Fig. 5 (left-hand panels). Here, CRSS values are constant regardless of the position of the aggregate (denoted by roman numerals) along path 1. By comparing the pole figures for the [100], [010] and [001] crystallographic axes between the A-type and *P*-dependent olivine fabrics, we observe a substantial decrease in their probability densities at a given position (e.g. position I) along path 1 which implies less prominent textures and hence, weaker anisotropy for the *P*-dependent fabric. In both A-type and *P*-dependent models, the pole figures almost do not vary for positions I, II and III. For instance, we observe the [100] axes to be subparallel to the direction of flow whereas the [010] axes are nearly normal to it at these positions. The crystallographic orientations of the *P*-dependent fabric appear slightly incoherent, almost existing in girdles. Upon the descent of the material from position IV to VI, pressure accumulation gradually switches the dominant slip activity from [100](010) to [001](010) (resembling a B-type fabric) making the [100] axes slightly fade away from a subparallel to a ∼45° from the flow direction.

As the olivine aggregate crosses the 410-km seismic discontinuity along path 1, the preferential orientations are erased and as a result, a weak texture is developed for wadsleyite across the UTZ. For this reason, we pick a different streamline (path 2 in Fig. 5) that completely navigates the UTZ to examine the texture evolution of wadsleyite. Results show that for all points along path 2, the distributions of the crystallographic axes almost remain unchanged for both fabric types. This is reasonable since the streamline is practically flat and the flow is mostly towards the $+x$ direction. Focusing on B_{wd}-type wadsleyite, the [001] axes tend to congregate towards the flow direction whereas the [100] axes are aligned perpendicular to it albeit more diffused than [001]. The [010] axes appear to be more dispersed. However, they exhibit slight sensitivity to changes in flow direction from positions IV through VI contrary to [100] and [001]. Primary and secondary strain accommodations at $<111>\{101\}$ and [001](010) slip systems, respectively are responsible for these orientations. As for a wet UTZ (i.e. C_{wd}-type fabric), orientations exhibit similar patterns with B_{wd}-type but with a significantly stronger texture (Ledoux *et al.* 2023).

We now examine the effect of *P*-induced olivine slip transitions and the choice of wadsleyite single crystal elastic constants constrained for dry (Núñez-Valdez *et al.* 2011, 2013) and hydrous wadsleyite (Zhou *et al.* 2022) onto the large-scale *S*-wave radial anisotropy ξ. To do so, we compare four mantle models, each of which is composed of an upper mantle fabric either with a *P*-dependent olivine (designated as ‘P-dep Ol’) or low pressure olivine (as ‘low-P Ol’) and a wet UTZ (as ‘Hyd Wd’) or dry UTZ (as ‘Dry Wd’). The specification of each model is tabulated in Table 4.

4.1 P-dep Ol + Hyd Wd

Fig. 6(a) displays the radial anisotropy before homogenization. Slightly faster V_{SV} are found just above 100 km with ξ close to unity. The most visible feature is the thick layer of positive radial anisotropy ($\xi \sim 1.04$) between 150 and 300 km. This is due to the heavy influence of the initial non-random textures acquired from the ridge model. Under the corner flow assumption, the ridge model loosely displays a low viscosity channel as evidenced by the confinement of large strains above ∼300 km (Hedjazian & Kaminski 2014). Boundary layer-type flow along this channel then produces strong signatures of positive ξ (Hedjazian & Kaminski 2014; Hedjazian *et al.* 2017; Kendall *et al.* 2022) which may then be inherited across the subplate mantle as aggregates get progressively sheared towards the trench (Fig. 6a). Between 300 and 410 km, we observe a very weak layer of negative radial anisotropy ($\xi \sim 0.99$). *P*-induced olivine slip transitions are solely responsible for such a distribution of radial anisotropy in the upper mantle. By considering a wet UTZ using a C_{wd}-type fabric and the single crystal elastic constants from Zhou *et al.* (2022) (410–520 km), we observe modest levels of negative radial anisotropy amounting to $\xi \sim 0.97$ away from the line of subduction. Next to this layer, there exists weak positive radial anisotropy ($\xi \sim 1.01$) which may reflect a change in the deformation pattern that includes rigid body rotation as soon as aggregates cross the 410-km phase transition boundary. Finally, very small amount of negative radial anisotropy, leaning towards $\xi \sim 1$ can be seen adjacent to the line of subduction indicating that monotonic deformation may not be sufficient to produce any CPO for a wadsleyite aggregate starting at a random texture at 410 km.

Fig. 6(b) shows the radial anisotropy after homogenization, that is, the large-scale/smooth version of ξ when sampled by a wavefield whose minimum wavelength is $\lambda_0 = 100$ km. Here, the general patterns of ξ are preserved. However, applying the tomographic operator removes small-scale spatial heterogeneities which eventually tones down the overall strength of radial anisotropy. This effect can be recognized in the spatial distribution of ξ in between 150 and 300 km and in between 410 and 520 km. It also replaces the sharp boundaries between positive and negative ξ with smoother transitions. Perhaps the most striking feature is the presence of positive ξ that traces the 410-km and 520-km seismic discontinuities. Here, horizontal isotropic layering (such as the 410 and 520 km discontinuities) induces positive extrinsic radial anisotropy ξ (∼1.02). The 520-km discontinuity though induces subdued levels of positive ξ compared to 410 km due to weaker contrasts in the polycrystal elastic moduli of the UTZ and the LTZ just above and below 520 km.

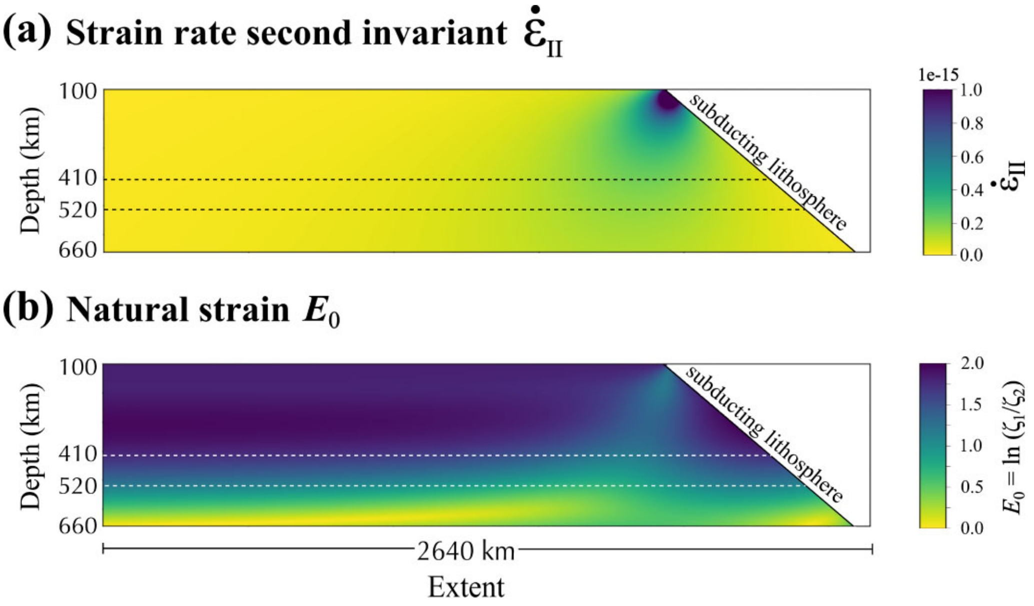

Figure 4. (a) Second invariant of the strain rate tensor $\dot{\varepsilon}_{II}$ and (b) magnitude of the finite strain tensor, also conventionally called natural strain E_0. At the initial time step, tracers are already deformed from a mid-ocean ridge model giving the characteristic well-distributed behaviour of E_0 in (b).

4.2 Low-P Ol + Hyd Wd

We next consider a model with an A-type olivine fabric corresponding to a dry upper mantle with slip system activities constrained at low pressures. Model Low-P Ol + Hyd Wd is characterized with a drastic increase in the amplitude of radial anisotropy $\xi > 1.1$ at ~220 km depth compared to P-dep Ol + Hyd Wd (Fig. 7a). In fact, the depth distribution of positive radial anisotropy encompasses the whole upper mantle (100–410 km), a direct consequence of a mantle model built from a single type of fabric. Next to the line of subduction, there exists a thin layer of negative radial anisotropy ($\xi \sim 0.95$) that is more prominent than in model P-dep Ol + Hyd Wd. Thus discounting *P*-induced slip transitions fosters continued strain accommodation by the [100](010) slip system (regardless of pressure changes) at each point along the stream line traced by the aggregate which in turn results in the overestimation of the strength of ξ and overextension of its vertical distribution. Upon homogenization, patterns of ξ are essentially the same in the upper mantle since the fast axes of seismic anisotropy are predominantly horizontal. A decrease in the strength of radial anisotropy can be observed adjacent to the line of subduction due to the non-linear spatial averaging of horizontal and vertical fast axes (Fig. 7b).

4.3 P-dep Ol + Dry Wd

With a dry UTZ represented by wadsleyite polycrystals built from B_{wd}-type textures and single crystal elastic constants from Núñez-Valdez *et al.* (2013), we predict faint amplitudes of negative radial anisotropy $\xi \sim 0.99$ in regions away from the line of subduction (Fig. 8a). The suppression in the strength of negative radial anisotropy in these regions can be explained by the apparent resistance of wadsleyite polycrystals to progressive shear deformation due to weaker activation of the primary slip system $<111>\{101\}$ of a B_{wd}-type fabric. Furthermore, the computed anisotropy not only depends on the texture but is also heavily influenced by the choice of the single crystal elastic constants used in the calculations. Upon homogenization, the extrinsic radial anisotropy delineating the 410-km discontinuity yields slightly higher intensities ($\xi \sim 1.035$) than in model P-dep Ol + Hyd Wd (Fig. 6b). Larger contrasts in seismic velocities due to the use of dry UTZ fabrics amplify the strength of extrinsic radial anisotropy in this mantle model.

4.4 Low-P Ol + Dry Wd

Our final mantle model consists of an upper mantle with an A-type olivine fabric and the same UTZ as in the preceding case. Similar to model P-dep Ol + Dry Wd, upon homogenization, we notice the amplification of extrinsic radial anisotropy along the 410-km seismic discontinuity due to large seismic velocity contrasts at the discontinuity (Fig. 9b). This results in the over-extension of the positive radial anisotropy ξ layer beyond 410 km and the inhibition of negative ξ across the UTZ.

5 DISCUSSION

5.1 Predictions of large-scale subplate and subslab radial anisotropy

Large-scale seismic anisotropy in the upper mantle (UM) and the upper transition zone (UTZ) have been associated with regions of strong deformation that is related to the preferential alignment of intrinsically anisotropic minerals or rock-scale mechanical layering brought by differentiation (e.g. Montagner 1998; Faccenda *et al.* 2019). To recap, maximum gradient of positive radial anisotropy ξ in the average UM lies at ~150 km which then gradually declines starting at ~200 km (e.g. Panning & Romanowicz 2006). The average UTZ, on the other hand, displays weak negative ξ probably due to the fact that most of the observed seismic anisotropy are confined close to subduction zones (Montagner *et al.* 2021). In the regional scale, radial anisotropy distributions in the UM and the UTZ are subjected to variations especially within the proximity of

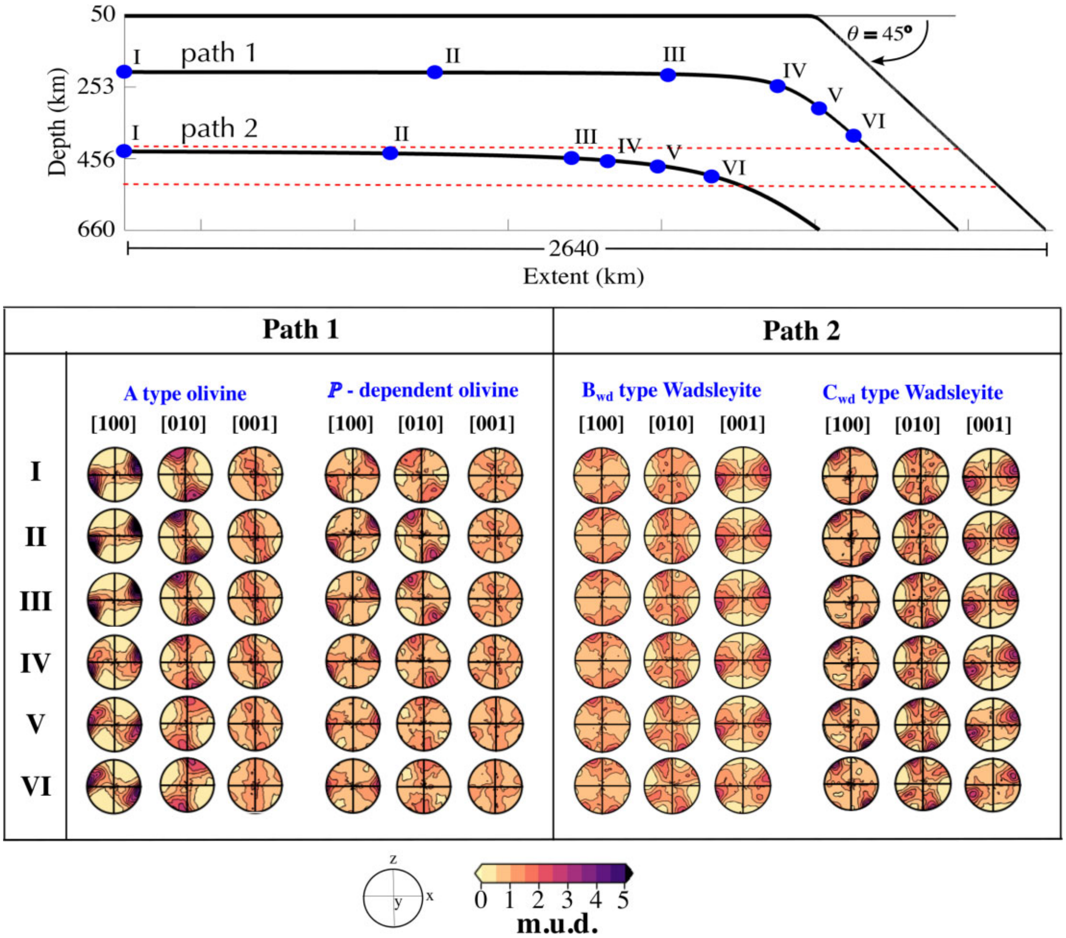

Figure 5. Development of CPO along streamlines traced by a plate-driven mantle flow. In the upper mantle (50–410 km), we study two cases of olivine CPO evolution along path 1:100 per cent A-type olivine (Tommasi *et al.* 2000, left-hand panels) versus 100 per cent *P*-dependent olivine (Raterron *et al.* 2014, middle panels). Across the upper transition zone (UTZ, 410–520 km), we consider the CPO evolution of B_{wd}- (i.e. dry) and C_{wd}-type (i.e. hydrous) wadsleyite along path 2. Provided are the multiples of uniform distribution (m.u.d.) for the [100], [010] and [001] crystallographic axes in stereographic projection at a given point (e.g. I, II, . . .) along paths 1 and 2. Dashed red lines mark the 410 and 520 km seismic discontinuities.

Table 4. Combined plasticity and elasticity models for olivine and wadsleyite used in the simulations. The garnet phase in the UTZ and the lower transition zone are deemed isotropic by imposing random textures. *PT*-dependent single crystal elastic constants of ringwoodite and garnet are taken from Sinogeikin *et al.* (2003) and Chai *et al.* (1997); Sinogeikin & Bass (2002), respectively.

Mantle model	Specifications			
	Upper mantle (100 per cent olivine)		Upper transition zone (60 per cent wadsleyite, 40 per cent garnet)	
	Ol fabric type	Ol elastic constants	Wd fabric type	Wd elastic constants
P-dep Ol + Hyd Wd	*P*-dependent CRSS	Mao *et al.* (2015)	C_{wd}-type	Zhou *et al.* (2022)
Low-P Ol + Hyd Wd	A-type	Mao *et al.* (2015)	C_{wd}-type	Zhou *et al.* (2022)
P-dep Ol + Dry Wd	*P*-dependent CRSS	Mao *et al.* (2015)	B_{wd}-type	Núñez-Valdez *et al.* (2011, 2013)
Low-P Ol + Dry Wd	A-type	Mao *et al.* (2015)	B_{wd}-type	Núñez-Valdez *et al.* (2011, 2013)

subduction zones due to several factors such as stronger deformation, bigger contribution in the modal abundance of the anisotropic phase and imbricated convection adjacent to stagnant slabs which impedes phase transformations of mid-mantle aggregates crossing the 660-km seismic discontinuity. The likely distribution of large-scale radial anisotropy ξ inferred from seismic observations are summarized in Fig. 10.

Our mantle models, albeit simple, still capture the general patterns of radial anisotropy to some extent. In models with *P*-induced olivine slip transitions, the UM is characterized by a positive radial anisotropy ξ down to a depth of ∼300 km in contrast to an A-type olivine fabric where the vertical distribution of positive ξ stretches down to the 410-km seismic discontinuity. Because of the continuity of flow underneath a mid-ocean ridge towards the subslab mantle, both mantle models already exhibit strong CPO at the initial time step of our current modelling domain. Our mantle models are therefore relevant beneath oceanic plates where steady-state flow may be anticipated; but may fail to explain CPO formation from transient flows such as regions proximal to migrating trenches, as well as the formation of frozen-in CPO across the lithosphere.

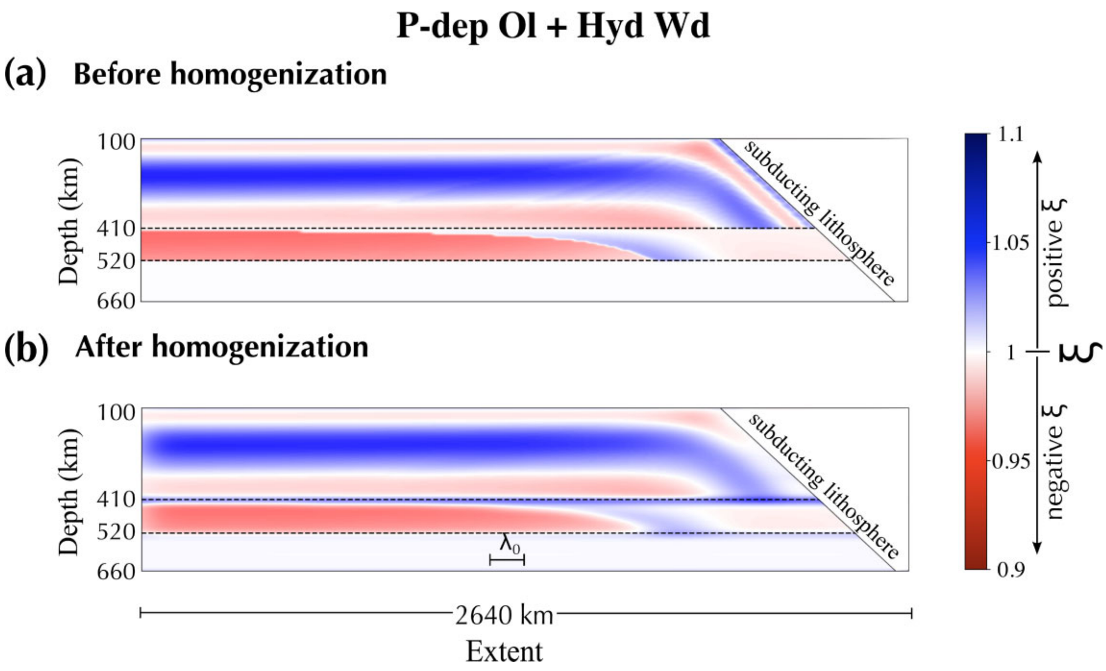

Figure 6. (a) Predicted *S*-wave radial anisotropy in terms of the parameter ξ for an upper-mantle consisting of 60 per cent *P*-dependent olivine aggregates, a wet upper transition zone (410–520 km) with 60 per cent C_{wd}-type wadsleyite and single crystal elastic constants from Zhou *et al.* (2022), and a seismically isotropic lower transition zone (520–660 km). (b) Long-wavelength equivalent of the predicted radial anisotropy in (a) using a homogenization wavelength of $\lambda_0 = 100$ km.

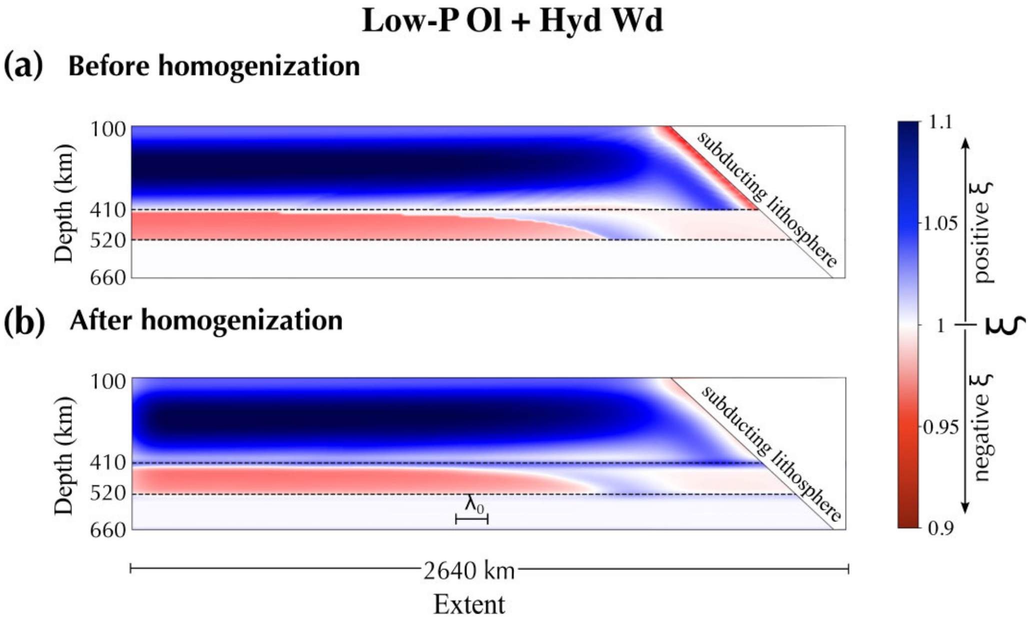

Figure 7. Same as Fig. 6 but with 60 per cent A-type olivine fabric for the upper mantle.

Upon homogenization, both models lose resolution power at scales smaller than $\lambda_0 = 100$ km which is the typical order of magnitude of the correlation length used in surface wave tomography (e.g. Debayle & Ricard 2013; Durand *et al.* 2015). The non-linear spatial averaging reduces the amplitude of radial anisotropy by a small amount in regions covered by the same pattern of ξ, and by a moderate to a large amount in regions where we observe both horizontal and vertical fast axes of anisotropy. This removes areas of sharp contrasts in ξ and replace them with smoother transitions. Even so, the effect of *P*-induced olivine slip transitions is still evident in the large-scale version of these mantle models. Thus, in light of our numerical simulations, the dependence of slip system activities with pressure prove to be a sensible candidate to explain the attenuation of the observed seismic anisotropy of the UM such as those found in the SEMUCB-WM1 (French & Romanowicz 2014) and SPiRaL (Simmons *et al.* 2021) global tomographic models.

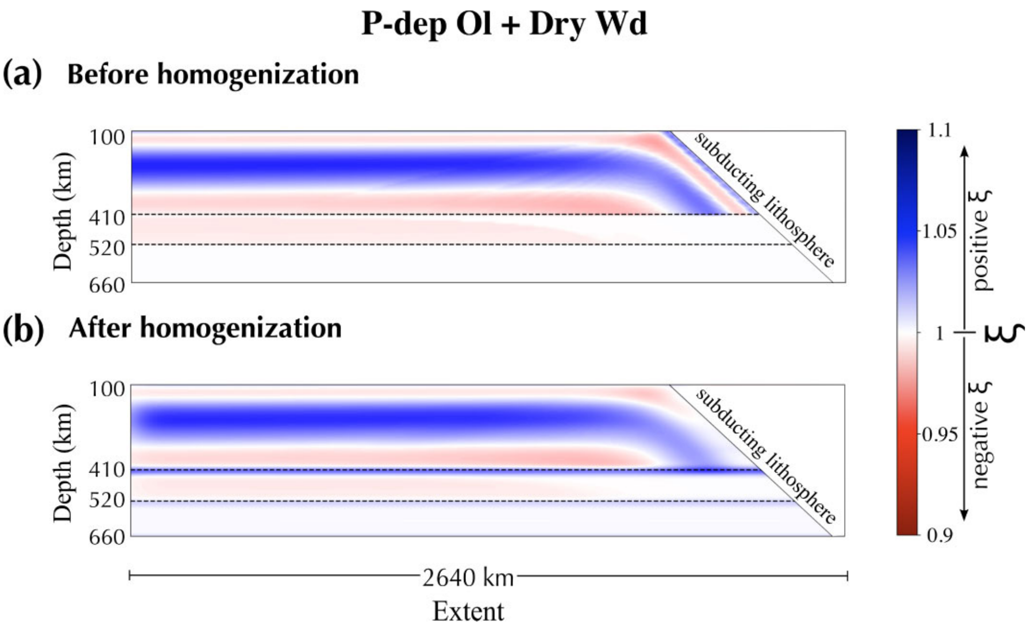

Figure 8. Same as Fig. 6 but with a dry upper transition zone (i.e. B_{wd}-type fabric and wadsleyite polycrystal elastic tensor built around the single crystal elastic constants of Núñez-Valdez *et al.* (2011, 2013).

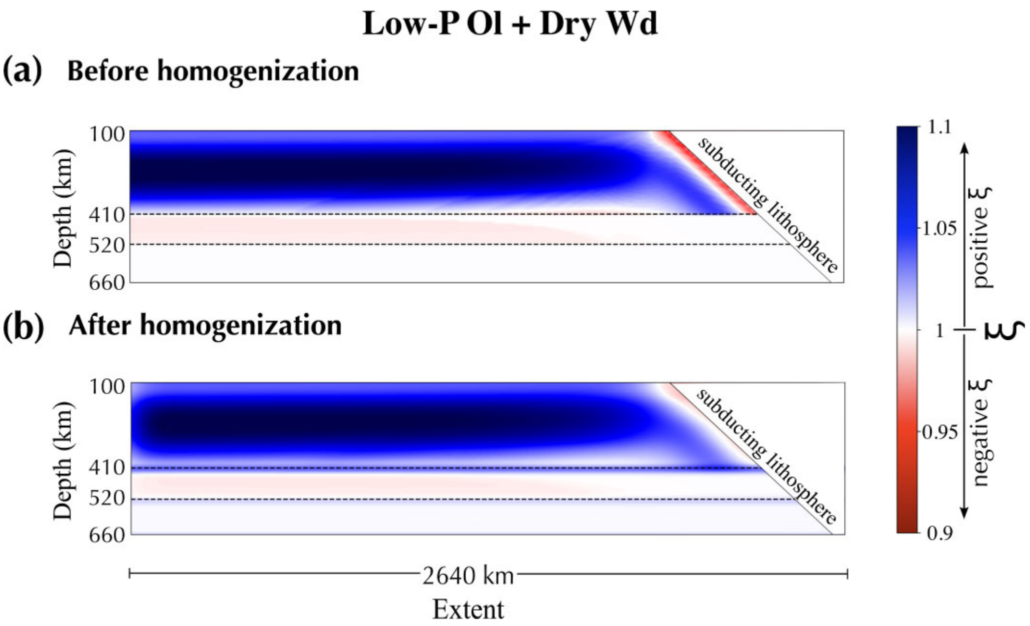

Figure 9. Same as Fig. 6 but with an A-type olivine for the upper mantle and a dry upper transition zone.

Probing deeper depths, the UTZ is generally characterized by a very weak negative radial anisotropy ξ assuming dry wadsleyite fabrics modelled from B_{wd}-type textures and single crystal elastic constants extrapolated from Núñez-Valdez *et al.* (2013), and by a moderate negative ξ when using wet fabrics [i.e. C_{wd}-type textures and single crystal elastic constants from Zhou *et al.* (2022)]. Indeed, the intrinsic seismic anisotropy present in the elastic tensor of an orthorhombic mineral such as wadsleyite controls the prediction of large-scale anisotropy apart from CPO. Nevertheless, the patterns of ξ are consistent with observations indicating the ubiquity of $c_{55} > c_{66}$ (i.e. after a tensor decomposition into an azimuthally averaged VTI tensor) across the ambient UTZ. Adjacent to the line of subduction, the region is nearly isotropic indicating the neglect of topotaxy in our simulations as the aggregates undergo P-induced phase transformation from olivine to wadsleyite at 410 km. To summarize, the strong sensitivity of wadsleyite elasticity on water content directly translates to significant variations in the amplitude of large-scale seismic anisotropy. As such, more experiments are probably required to fully understand the effect of water on elasticity and hence, be integrated in computational models of mantle anisotropy. This offers an opportunity to constrain the deformation patterns associated with water-rich minerals in the mantle transition zone thanks to these empirical data and computational models.

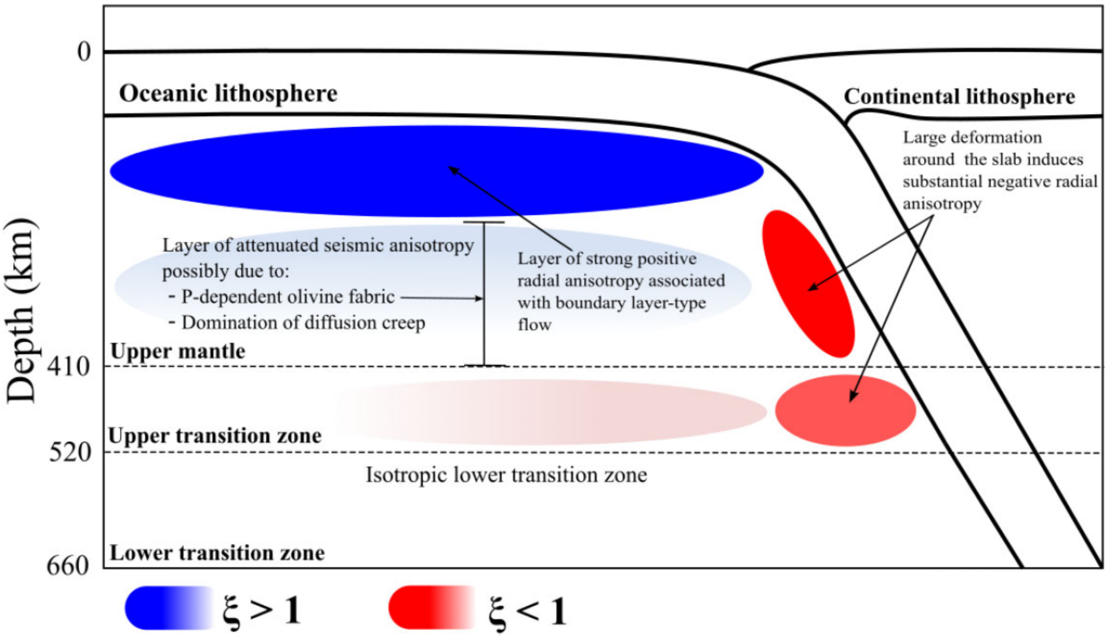

Figure 10. Diagram depicting the likely spatial distribution of large-scale subplate and subslab radial anisotropy ξ inferred from tomographic observations. Regions in blue pertain to positive radial anisotropy ($\xi > 1$) whereas those in red denote negative radial anisotropy ($\xi < 1$) with colour gradients representing their strength.

5.2 Layering-induced extrinsic anisotropy at 410 km

At least two conditions must be satisfied to generate extrinsic anisotropy from small-scale isotropic heterogeneities: (1) when seismic velocity contrasts are large and (2) when the minimum wavelength of the observed wavefield is larger than the scale of the heterogeneities. Imaging phase transition boundaries with long-period seismic waves is a particularly interesting subject as it may meet such criteria. For example, average 1-D profiles of radial anisotropy ξ underneath the Indian Ocean recovered from the inversion of phase velocity measurements show a positive gradient of ξ at roughly $\sim$410-km depth which almost vanishes upon the inclusion of group velocity data (Weidner *et al.* 2022). Ricard *et al.* (2005) showed that seismic velocity variations could reach at most 5% at the 410-km boundary as seen in synthetic tomography images constructed from mineral physics and thermodynamic calculations. Based on the empirical results of Alder *et al.* (2017), this produces up to 1 per cent extrinsic radial anisotropy ξ which is in good agreement with the extrinsic ξ produced at 410 km from our mantle model with a hydrous UTZ. Interestingly, Faccenda *et al.* (2019) also showed that major phase transitions produce up to 1 per cent positive radial anisotropy that is extrinsic in origin. Meanwhile, a dry UTZ, based on our computations, tends to produce up to 3 per cent extrinsic ξ at 410 km. Such observations are reasonable since dry fabrics tend to exhibit larger seismic velocities than hydrous ones, and hence, sharper velocity contrasts at 410 km. Based on our results, this begs the question of whether layering-induced extrinsic anisotropy at phase transition boundaries could be a good first-order proxy to estimate the amount of water present in the mantle transition zone. Further tests are therefore required which is beyond the scope of this study.

5.3 Comparison with observations of average radial anisotropy versus depth

For each homogenized radial anisotropy model presented in the previous section, we take its horizontal average, plot it with depth and then compare it with global tomographic observations of ξ derived from Visser *et al.* (2008), SEMUCB-WM1 (French & Romanowicz 2014) and SPiRaL (Simmons *et al.* 2021; Fig. 11). Across the UM, our models with A-type olivine fabric (solid green and dashed orange lines) predict ξ values that strongly deviate from tomographic observations. Contrastingly, those with *P*-induced olivine slip transitions (solid blue and dashed red lines) predict values comparable to tomographic observations. From this, we again reiterate that *P*-dependent fabrics modulate the strength of large-scale radial anisotropy similar to mantle models with composite rheologies and low grain boundary mobility values corresponding to slow-developing textures such as in Hedjazian *et al.* (2017). Our mantle models, both of the *P*-dependent and A-type kind exhibit maximum ξ strength at $\sim$220 km different from observations which are typically located at $\sim$100–150 km depth. This may result from the simplicity of our mantle flow model where we only consider the strain rate-dependence of the effective viscosity. In reality, the rheology of the mantle depends on several factors including temperature, pressure and grain size (e.g. Hirth & Kohlstedt 2003). Both pressure and grain size regulate the relative strength of diffusion versus dislocation creep mechanisms, and the temperature increase with depth across the subplate mantle tends to decrease the effective viscosity (Mainprice 2007). As a result, this repositions the vertical distribution of the low viscosity channel depending on the values of these rheological parameters and in turn, also the vertical distribution of positive ξ.

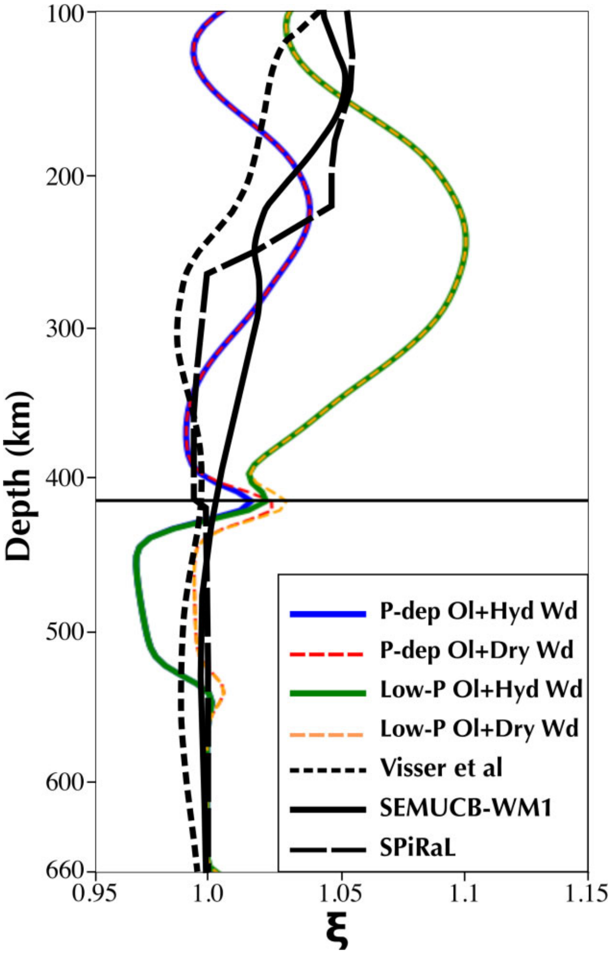

Figure 11. Comparison between 1-D depth profiles of average radial anisotropy from models P-dep Ol + Hyd Wd, P-dep Ol + Dry Wd, Low-P Ol + Hyd Wd and Low-P Ol + Dry Wd. Superimposed are globally averaged radial anisotropy profiles derived from tomographic models Visser *et al.* (2008), SEMUCB-WM1 (French & Romanowicz 2014), and SPiRaL (Simmons *et al.* 2021). Even with a simple geodynamic setup, introducing *P*- −dependent fabrics fit the observations to some extent. Contrastingly, using a single fabric type clearly overestimates the strength of anisotropy.

Across the UTZ, using dry wadsleyite (for both elasticity and plasticity) appear to fit tomographic observations of ξ (i.e. Visser *et al.* 2008, SEMUCB-WM1 and SPiRaL) more effectively than hydrous wadsleyite (Fig. 11). Zhou *et al.* (2022) found that regions close to subducting slabs exhibit higher water content than the rest of the ambient UTZ. Keep in mind that the observations of ξ displayed here are global averages of Visser *et al.* (2008), French & Romanowicz (2014) and Simmons *et al.* (2021). As such, the areas underneath oceanic and continental lithospheres that are relatively dry occupy a larger volume than convergent margins resulting in smaller amplitudes of negative radial anisotropy ($\xi < 1$) when globally averaged. Because our mantle models with dry UTZ fabrics tend to produce weaker levels of radial anisotropy, this may sufficiently explain why it matches the observations better than the other.

5.4 On the influence of pressure and the decrease in anisotropy past ∼150 km depth

Our results show that one can model a decrease in radial anisotropy strength past ∼150 km due to the role of hydrostatic pressure in the large-scale imprint of mantle fabric transitions (i.e. radial anisotropy distribution) as proposed by Raterron *et al.* (2007) and Mainprice *et al.* (2005). In retrospect, Karato *et al.* (2008) argued, however, that there was insufficient evidence that pressure has an intrinsic influence on olivine slip transitions. This is because deformation experiments in olivine at high pressures were also characterized by relatively high deviatoric stresses which could have potentially altered its microstructures (see Hansen *et al.* 2021, for a review). From a modelling standpoint, this has led to the association of the decrease in anisotropy principally in terms of changes in the dominant creeping mechanism at the base of the upper mantle (e.g. Karato & Wu 1993; Behn *et al.* 2009; Hedjazian *et al.* 2017). Even so, one could not completely rule out the intrinsic influence of pressure as it has been demonstrated that even at high deviatoric stresses, olivine deforms primarily via dislocation creep rather than low-temperature plasticity as initially hypothesized by Goetze & Poirier (1978). Furthermore, fabric transitions due to pressure influence could also be an active process at differential stresses reminiscent of that of the deep upper mantle (Raterron *et al.* 2012). While we acknowledge pressure influence on CPO is a disputed topic, our goal is not to reconcile both explanations for it; rather, we solely perform a test of the hypothesis on how changes in pressure affect CPO evolution, and ultimately, the distribution of large-scale anisotropy.

The geodynamic model implemented in this study involves an asthenosphere that is passively deformed by a moving oceanic plate which fosters a symmetric distribution of deformation laterally and with depth (Figure 4b). However, active upwelling and lateral spreading of mantle materials could be present, at least locally, which cannot be replicated using passive models of mantle flow. Masalu (2007) reported that faster-moving plates such as those observed across the Pacific-Antarctic and Pacific-Nazca ridges tend to generate shallow-rooted convection cells. This would subsequently introduce local disturbances that could potentially increase the magnitude of velocity gradients leading to a decrease in dislocation creep viscosity. This process would then develop a deeper anisotropy than underneath slow-moving plates although its vertical distribution would still likely be confined in the upper ∼300 km of the asthenosphere (Kendall *et al.* 2022). Finally, lateral variations in pressure could prompt active channel flow within the upper mantle which could facilitate trench and slab migration (Heuret & Lallemand 2005). While subduction style and its corresponding mode switching depend on migration velocities (e.g. Agrusta *et al.* 2017), Sturgeon *et al.* (2019) predicted that asthenospheric anisotropy would also not exceed ∼300 km.

As stated earlier, the employed homogenization technique delivers an effective medium that is compatible with a tomographic model obtained from a full waveform inversion assuming perfect data coverage. Upper mantle (an)isotropic structure, however, is traditionally illuminated using surface waves since most of its energy is concentrated close to the Earth's surface. As it is extracted from the low-frequency component of the seismogram, surface wave tomography offers the capability to robustly capture the long-wavelength lateral *S*-wave structure, including the azimuthal and radial components of its anisotropy. When using its fundamental mode, however, surface tomography yields poor vertical resolution below ∼300 km due to its decreasing sensitivity with depth (e.g. Bodin *et al.* 2015). Because of this, the weakening in the strength of anisotropy observed in the deep upper mantle could partly be explained by the decrease of the sensitivity of surface waves with depth. Thankfully, modern advances in surface wave tomography incorporate overtone data which then greatly increases its depth coverage such as down to the mantle transition zone (e.g. Debayle & Ricard 2012; Montagner *et al.* 2021). It is thus safe to assume that long-period tomography cannot completely explain the decline in anisotropy, especially with the recent implementation of techniques that automatically update tomographic models upon the increase in the amount of available seismic data (e.g. Debayle *et al.* 2016).

5.5 Modelling limitations

This work is not intended to comprehensively examine the origins of large-scale radial anisotropy in the upper and mid-mantle. It, instead, serves as a foundation of implementing a multiscale approach that incorporates P-induced olivine slip transitions and strain-induced seismic anisotropy computation of polycrystalline wadsleyite using its most recent dislocation slip systems. Our method is applied in a simple geodynamic setup of a 2-D plate-driven motion with non-Newtonian rheology. Barring the simplicity of our geodynamic model, we acknowledge some of the most important limitations our approach does not cover.

Firstly, our models of the upper mantle (UM) large-scale radial anisotropy ξ disregard the contribution of pyroxene phases in the aggregates. By modelling the CPO of such phases, we anticipate the total seismic anisotropy within the aggregate to be changed to some degree (Maupin *et al.* 2007). A pyrolitic upper mantle, for instance, constitutes 60 per cent olivine and 40 per cent pyroxene (Ringwood 1962). The 40 per cent coming from the pyroxene phase would likely contradict the preferential alignment of the [100] crystallographic axes of the olivine phase resulting in the dilution of the strength of anisotropy (Tommasi *et al.* 2000). Regardless, the patterns of the large-scale version of seismic anisotropy in our pyrolitic mantle model, or any other model composition of periodotite as long as the bulk of its volume fraction is allocated to olivine, are consistent, to first-order, with observations.

Secondly, the average seismic anisotropy in the transition zone (TZ) cannot be reproduced by the hypothesized TZ fabrics with a marginally anisotropic UTZ and anisotropic LTZ in a subduction zone setting (Montagner & Kennett 1996; Visser *et al.* 2008; Yuan & Beghein 2013; French & Romanowicz 2014). Fortunately, the effective medium averaging of Capdeville *et al.* (2015) accounts for extrinsic anisotropy due to structural layering. Such structures may be brought by the differentiation of the subducting crust into enriched layers of garnet and ringwoodite (Karato 1998). In our mantle models, we have demonstrated the production of layering-induced extrinsic anisotropy resulting from the 410- and 520-km seismic discontinuities. Apart from this, we also could not rule out the existence of other intrinsically anisotropic mineral phases such as akimotoite. Shiraishi *et al.* (2008) performed deformation experiments on such minerals and found the existence of substantial CPO at small strains. Recently, Guan *et al.* (2022) conducted another deformation experiment on akimotoite, but this time at PT conditions relevant to regions close to a cold subducting slab in the LTZ. There they found that the observed seismic anisotropy at these depths can be explained by the CPO of akimotoite. Notwithstanding such experiments, however, it is still a subject of debate whether the strains are large enough to produce such a CPO when the slab is often characterized as rigid and poorly deforming.

Finally, although we addressed the issue of limited frequency band of seismic data to tomographic filter our mantle models, we have done so assuming perfect ray path coverage. An additional preprocessing step is required to account for the inhomogeneous distribution of source-station pairs by constructing a resolution matrix $\mathcal{R}$ and then subsequently applied to our mantle models (Simmons *et al.* 2019). Recently, Kendall *et al.* (2022) implemented such a technique using the SGLOBE-Rani tomographic filter (Chang *et al.* 2015) to study the effect of tectonic stresses on large-scale radial anisotropy underneath ridges. They, however, neglected finite frequency effects. One future avenue to explore is the implementation of both methods to improve the comparison between the predicted seismic anisotropy and observations. Furthermore, most long-period tomographic schemes are inferred from seismic data that possess variable sensitivity to certain structures. Surface wave tomography, for instance, possesses variable sensitivity with depth. Our current homogenization technique, however, precludes variable sensitivity and is instead fixed across the whole domain. A future improvement of the work is to implement variable homogenization wavelengths which could provide a more useful comparison with tomographic models.

6 CONCLUSION

We have presented a method that integrates the effect of pressure on mineral phases, slip systems, and elastic properties down to 520-km depth within the VPSC approach combined with simple flow models and elastic homogenization approach. The method is applied to compute the strain-induced seismic anisotropy coming from a 2-D plate-driven corner flow model with a non-Newtonian (n = 3) rheology. We then apply a tomographic filter based on a non-periodic homogenization approach to account for finite-frequency seismic data, and then view our computational models as a seismic tomography image assuming perfect data coverage.

Contrary to common practice that computes CPO using a single type of mantle fabric, implementing slip system CRSS as a function of pressure allows for the evolution of mantle fabrics with variations in pressure. Thus when implemented with realistic geodynamic models in the future, the Lagrangian approach can be applied to follow not only the trajectory of the aggregate but also keep track of its texture evolution in response to changes in dynamic pressure. The method can now be expanded to more complex geodynamic settings such as exploring the origins of the observed seismic anisotropy associated with strong deformation around a subduction zone. Still, even when coupled with a simple mantle corner flow model, we report the capability of our technique to produce radial anisotropy patterns that resemble global tomographic observations.

Unlike using a single fabric type (e.g. A-type olivine), P-induced olivine slip transitions allow for the weakening of ξ with depth in the upper mantle. Further testing, of course, is required to support this finding, particularly in realistic geodynamic settings where complex deformation patterns may obscure the distribution of large-scale anisotropy. With the correct choice of wadsleyite elastic constants, the CPO coming from the newly constrained dislocation slip systems of wadsleyite reproduces the ubiquity of negative ξ observed in tomographic models of the upper transition zone.

AUTHOR CONTRIBUTIONS

J. K. Magali (Conceptualization [Lead], Formal analysis [Lead], Investigation [Lead], Methodology [Lead], Software [Equal], Writing – original draft [Lead], Writing – review and editing [Equal]), E. E. Ledoux (Data curation [Lead], Writing – review and editing [Supporting]), C. Thomas (Funding acquisition [Equal], Project administration [Equal], Resources [Equal], Supervision [Equal], Writing – review and editing [Equal]), Y. Capdeville (Methodology [Equal], Software [Equal], Writing – review and editing [Supporting]), and

S. Merkel (Conceptualization [Supporting], Investigation [Supporting], Methodology [Supporting], Project administration [Lead], Resources [Lead], Software [Supporting], Supervision [Lead], Writing – review and editing [Equal])

ACKNOWLEDGMENTS

The study was mainly financed by the bilateral ANR-DFG TIMEleSS project (ANR-17-CE31-0025; TH 1530/18-1; SA 2585/3-1; SP1216/8-1), and in part by the DFG LASSIE project (TH1530/24-1). Computations were performed on the Mésocentre de Calcul Scientifique Intensif de l'Université de Lille and the in-house PALMA cluster of the University of Münster.

DATA AVAILABILITY

While the VPSC source code is not publicly available, its modified version (i.e. pressure-dependent fabric calculations) together with its input files can be provided by the corresponding author (jkvmagali@gmail.com). The Fast Fourier Homogenization (FFH) algorithm can be made available upon reasonable request to Y. Capdeville. Its foundation is based upon the following in-text citation references: Capdeville *et al.* (2015) and Capdeville & Métivier (2018). This study is entirely numerical. No data have been produced for this work.

REFERENCES

Agrusta, R., Goes, S. & Van Hunen, J., 2017. Subducting-slab transition-zone interaction: Stagnation, penetration and mode switches, *Earth planet. Sci. Lett.,* **464,** 10–23.

Alder, C., Bodin, T., Ricard, Y., Capdeville, Y., Debayle, E. & Montagner, J., 2017. Quantifying seismic anisotropy induced by small-scale chemical heterogeneities, *Geophys. J. Int.,* **211**(3), 1585–1600.

Allaire, G., 1992. Homogenization and two-scale convergence, *SIAM J. Math. Anal.,* **23**(6), 1482–1518.

Auer, L., Becker, T.W., Boschi, L. & Schmerr, N., 2015. Thermal structure, radial anisotropy, and dynamics of oceanic boundary layers, *Geophys. Res. Lett.,* **42**(22), 9740–9749.

Backus, G.E., 1962. Long-wave elastic anisotropy produced by horizontal layering, *J. geophys. Res.,* **67**(11), 4427–4440.

Batchelor, G.K., 2000. *An Introduction to Fluid Dynamics,* Cambridge Univ. Press.

Behn, M.D., Hirth, G. & Elsenbeck II, J.R., 2009. Implications of grain size evolution on the seismic structure of the oceanic upper mantle, *Earth planet. Sci. Lett.,* **282**(1-4), 178–189.

Bensoussan, A., Lions, J.-L. & Papanicolaou, G., 2011. *Asymptotic Analysis For Periodic Structures,* Vol. **374,** American Mathematical Soc..

Blanc, X., Le Bris, C. & Lions, P.-L., 2007. Stochastic homogenization and random lattices, *Journal de mathématiques pures et appliquées,* **88**(1), 34–63.

Bodin, T., Capdeville, Y., Romanowicz, B. & Montagner, J.-P., 2015. Interpreting radial anisotropy in global and regional tomographic models, in *The Earth's Heterogeneous Mantle,* Springer, pp. 105–144.

Boneh, Y., Morales, L.F., Kaminski, E. & Skemer, P., 2015. Modeling olivine cpo evolution with complex deformation histories: Implications for the interpretation of seismic anisotropy in the mantle, *Geochem. Geophys. Geosyst.,* **16**(10), 3436–3455.

Boschi, L. & Ekström, G., 2002. New images of the earth's upper mantle from measurements of surface wave phase velocity anomalies, *J. geophys. Res.,* **107**(B4), ESE–1.

Browaeys, J.T. & Chevrot, S., 2004. Decomposition of the elastic tensor and geophysical applications, *Geophys. J. Int.,* **159**(2), 667–678.

Capdeville, Y. & Marigo, J.-J., 2007. Second order homogenization of the elastic wave equation for non-periodic layered media, *Geophys. J. Int.,* **170**(2), 823–838.

Capdeville, Y. & Métivier, L., 2018. Elastic full waveform inversion based on the homogenization method: theoretical framework and 2-D numerical illustrations, *Geophys. J. Int.,* **213,** 1093–1112.

Capdeville, Y., Guillot, L. & Marigo, J.-J., 2010. 2-D non-periodic homogenization to upscale elastic media for P–SV waves, *Geophys. J. Int.,* **182**(2), 903–922.

Capdeville, Y., Zhao, M. & Cupillard, P., 2015. Fast Fourier homogenization for elastic wave propagation in complex media, *Wave Motion,* **54,** 170–186.

Castelnau, O., Blackman, D., Lebensohn, R. & Ponte Castañeda, P., 2008. Micromechanical modeling of the viscoplastic behavior of olivine, *J. geophys. Res.,* **113**(B9), doi:10.1029/2007JB005444.

Castelnau, O., Cordier, P., Lebensohn, R.A., Merkel, S. & Raterron, P., 2010. Microstructures and rheology of the earth's upper mantle inferred from a multiscale approach, *Comptes Rendus Physique,* **11**(3-4), 304–315.

Chai, M., Brown, J.M. & Slutsky, L.J., 1997. The elastic constants of a pyrope-grossular-almandine garnet to 20 gpa, *Geophys. Res. Lett.,* **24**(5), 523–526.

Chang, S.-J., Ferreira, A.M., Ritsema, J., van Heijst, H.J. & Woodhouse, J.H., 2015. Joint inversion for global isotropic and radially anisotropic mantle structure including crustal thickness perturbations, *J. geophys. Res.,* **120**(6), 4278–4300.

Christensen, U.R., 1996. The influence of trench migration on slab penetration into the lower mantle, *Earth planet. Sci. Lett.,* **140**(1-4), 27–39.

Couvy, H., Frost, D.J., Heidelbach, F., Nyilas, K., Ungar, T., Mackwell, S. & Cordier, P., 2004. Shear deformation experiments of Forsterite at 11 GPa-1400 C in the multianvil apparatus, *Eur. J. Mineral.,* **16**(6), 877–889.

Crampin, S., 1994. The fracture criticality of crustal rocks, *Geophys. J. Int.,* **118**(2), 428–438.

Debayle, E. & Ricard, Y., 2012. A global shear velocity model of the upper mantle from fundamental and higher Rayleigh mode measurements, *J. geophys. Res.,* **117**(B10), doi:10.1029/2012JB009288.

Debayle, E. & Ricard, Y., 2013. Seismic observations of large-scale deformation at the bottom of fast-moving plates, *Earth planet. Sci. Lett.,* **376,** 165–177.

Debayle, E., Bodin, T., Durand, S. & Ricard, Y., 2020. Seismic evidence for partial melt below tectonic plates, *Nature,* **586**(7830), 555–559.

Debayle, E., Dubuffet, F. & Durand, S., 2016. An automatically updated s-wave model of the upper mantle and the depth extent of azimuthal anisotropy, *Geophys. Res. Lett.,* **43**(2), 674–682.

Demouchy, S., Mainprice, D., Tommasi, A., Couvy, H., Barou, F., Frost, D.J. & Cordier, P., 2011. Forsterite to wadsleyite phase transformation under shear stress and consequences for the earth's mantle transition zone, *Phys. Earth planet. Inter.,* **184**(1-2), 91–104.

Durand, S., Debayle, E. & Ricard, Y., 2015. Rayleigh wave phase velocity and error maps up to the fifth overtone, *Geophys. Res. Lett.,* **42**(9), 3266–3272.

Durinck, J., Carrez, P. & Cordier, P., 2007. Application of the peierls-nabarro model to dislocations in forsterite, *Eur. J. Mineral.,* **19**(5), 631–639.

Dziewonski, A.M. & Anderson, D.L., 1981. Preliminary reference earth model, *Phys. Earth planet. Inter.,* **25**(4), 297–356.

Eddy, C.L., Ekström, G. & Nettles, M., 2022. Three-dimensional seismic anisotropy in the Pacific upper mantle from inversion of a surface-wave dispersion dataset, *Geophys. J. Int.,* **231**(1), 355–383.

Faccenda, M. & Capitanio, F.A., 2012. Development of mantle seismic anisotropy during subduction-induced 3-D flow, *Geophys. Res. Lett.,* **39**(11), doi:10.1029/2012GL051988.

Faccenda, M. & Capitanio, F.A., 2013. Seismic anisotropy around subduction zones: insights from three-dimensional modeling of upper mantle deformation and sks splitting calculations, *Geochem. Geophys. Geosyst.,* **14**(1), 243–262.

Faccenda, M., 2014. Mid mantle seismic anisotropy around subduction zones, *Phys. Earth planet. Inter.,* **227,** 1–19.

Faccenda, M., Ferreira, A.M., Tisato, N., Lithgow-Bertelloni, C., Stixrude, L. & Pennacchioni, G., 2019. Extrinsic elastic anisotropy in a compositionally heterogeneous earth's mantle, *J. geophys. Res.,* **124**(2), 1671–1687.

Ferreira, A.M., Faccenda, M., Sturgeon, W., Chang, S.-J. & Schardong, L., 2019. Ubiquitous lower-mantle anisotropy beneath subduction zones, *Nat. Geosci.,* **12**(4), 301–306.

Fischer, K.M. & Wiens, D.A., 1996. The depth distribution of mantle anisotropy beneath the Tonga subduction zone, *Earth planet. Sci. Lett.,* **142**(1-2), 253–260.

Fraters, M. R.T. & Billen, M.I., 2021. On the implementation and usability of cpo evolution in geodynamic modelling, *Geochem., Geophys., Geosyst.,* **22**(10), doi:10.1029/2021GC009846.

French, S. & Romanowicz, B.A., 2014. Whole-mantle radially anisotropic shear velocity structure from spectral-element waveform tomography, *Geophys. J. Int.,* **199**(3), 1303–1327.

Girard, J., Silber, R.E., Mohiuddin, A., Chen, H. & Karato, S.-i., 2020. Development of a stress sensor for in-situ high-pressure deformation experiments using radial x-ray diffraction, *Minerals,* **10**(2), doi:10.3390/min10020166.

Goetze, C. & Poirier, J., 1978. The mechanisms of creep in olivine [and discussion], philos, *Philos. Trans. R. Soc., A,* **288**(1350), 99–119.

Guan, L., Yamazaki, D., Tsujino, N., Tange, Y. & Higo, Y., 2022. Seismic anisotropy in the lower mantle transition zone induced by lattice preferred orientation of akimotoite, *Geophys. Res. Lett.,* **49**(11), e2022GL098549.

Guillot, L., Capdeville, Y. & Marigo, J.-J., 2010. 2-d non-periodic homogenization of the elastic wave equation: Sh case, *Geophys. J. Int.,* **182**(3), 1438–1454.

Gung, Y., Panning, M. & Romanowicz, B., 2003. Global anisotropy and the thickness of continents, *Nature,* **422**(6933), 707–711.

Hansen, L.N., Faccenda, M. & Warren, J.M., 2021. A review of mechanisms generating seismic anisotropy in the upper mantle, *Phys. Earth planet. Inter.,* **313,** doi:10.1016/j.pepi.2021.106662.

Hashin, Z. & Shtrikman, S., 1963. A variational approach to the elastic behavior of multiphase materials, *J. Mech. Phys. Solids,* **11**(2), 127–140.

Hedjazian, N. & Kaminski, E., 2014. Defining a proxy for the interpretation of seismic anisotropy in non-Newtonian mantle flows, *Geophys. Res. Lett.,* **41**(20), 7065–7072.

Hedjazian, N., Capdeville, Y. & Bodin, T., 2021. Multiscale seismic imaging with inverse homogenization, *Geophys. J. Int.,* **226**(1), 676–691.

Hedjazian, N., Garel, F., Davies, D.R. & Kaminski, E., 2017. Age-independent seismic anisotropy under oceanic plates explained by strain history in the asthenosphere, *Earth planet. Sci. Lett.,* **460,** 135–142.

Heuret, A. & Lallemand, S., 2005. Plate motions, slab dynamics and back-arc deformation, *Phys. Earth planet. Inter.,* **149**(1-2), 31–51.

Hirth, G. & Kohlstedt, D., 2003. Rheology of the upper mantle and the mantle wedge: a view from the experimentalists, *Geophys. Monog.-Am. Geophys. Un.,* **138,** 83–106.

Hornby, B.E., Schwartz, L.M. & Hudson, J.A., 1994. Anisotropic effective-medium modeling of the elastic properties of shales, *Geophysics,* **59**(10), 1570–1583.

Jung, H., Mo, W. & Green, H.W., 2009. Upper mantle seismic anisotropy resulting from pressure-induced slip transition in olivine, *Nat. Geosci.,* **2**(1), 73–77.

Kaneshima, S. & Silver, P.G., 1992. A search for source side mantle anisotropy, *Geophys. Res. Lett.,* **19**(10), 1049–1052.

Karato, S.-i. & Wu, P., 1993. Rheology of the upper mantle: a synthesis, *Science,* **260**(5109), 771–778.

Karato, S.-i., 1998. Seismic anisotropy in the deep mantle, boundary layers and the geometry of mantle convection, in *Geodynamics of Lithosphere & Earth's Mantle: Seismic Anisotropy as a Record of the Past and Present Dynamic Processes,* pp. 565–587, eds Plomerová, J., Liebermann, R.C. & Babuška, V., Springer.

Karato, S.-i., Jung, H., Katayama, I. & Skemer, P., 2008. Geodynamic significance of seismic anisotropy of the upper mantle: new insights from laboratory studies, *Annu. Rev. Earth planet. Sci.,* **36,** 59–95.

Katsura, T. *et al.*, 2004. Olivine-wadsleyite transition in the system (Mg, Fe) 2SiO$_4$, *J. geophys. Res.,* **109**(B2), doi:10.1029/2003JB002438.

Kawazoe, T., Ohuchi, T., Nishihara, Y., Nishiyama, N., Fujino, K. & Irifune, T., 2013. Seismic anisotropy in the mantle transition zone induced by shear deformation of wadsleyite, *Phys. Earth planet. Inter.,* **216,** 91–98.

Kendall, E., Faccenda, M., Ferreira, A. & Chang, S.-J., 2022. On the relationship between oceanic plate speed, tectonic stress, and seismic anisotropy, *Geophys. Res. Lett.,* **49**(15), e2022GL097795.

Kendall, J. & Silver, P., 1998. Investigating causes of d" anisotropy, in *The Core-Mantle Boundary Region,* Vol. **28,** pp. 97–118, eds Gurnis, M., Wysession, M.E., Knittle, E. & Buffett, B.A., AGU.

Kumazawa, M. & Anderson, O.L., 1969. Elastic moduli, pressure derivatives, and temperature derivatives of single-crystal olivine and single-crystal forsterite, *J. geophys. Res.,* **74**(25), 5961–5972.

Lebensohn, R.A. & Tomé, C., 1993. A self-consistent anisotropic approach for the simulation of plastic deformation and texture development of polycrystals: application to zirconium alloys, *Acta Metall. Mater.,* **41**(9), 2611–2624.

Ledoux, E.E. *et al.* , 2023. In-situ study of microstructures induced by the olivine to wadsleyite transformation at conditions of the 410 km depth discontinuity, *Am. Min.,* **108**(12), 2283–2293.

Ledoux, E.E. *et al.*, 2023. Deformation mechanisms, microstructures, and seismic anisotropy of wadsleyite in the earth's transition zone, *Geochem. Geophys. Geosyst.,* **24**(11), e2023GC011026.

Li, Q., Li, Z.-H. & Zhong, X., 2022. Overriding lithospheric strength affects continental collisional mode selection and subduction transference: Implications for the greater india–asia convergent system, *Front. Earth Sci.,* **10,** 919174.

Li, Z.-H., Di Leo, J.F. & Ribe, N.M., 2014. Subduction-induced mantle flow, finite strain, and seismic anisotropy: numerical modeling, *J. geophys. Res.,* **119**(6), 5052–5076.

MacDougall, J.G., Jadamec, M.A. & Fischer, K.M., 2017. The zone of influence of the subducting slab in the asthenospheric mantle, *J. geophys. Res.,* **122**(8), 6599–6624.

Magali, J.K., Bodin, T., Hedjazian, N., Samuel, H. & Atkins, S., 2021. Geodynamic tomography: constraining upper-mantle deformation patterns from Bayesian inversion of surface waves, *Geophys. J. Int.,* **224**(3), 2077–2099.

Magali, J.K., Bodin, T., Hedjazian, N., Ricard, Y., Capdeville, Y. & Debayle, E., 2021. Quantifying intrinsic and extrinsic contributions to radial anisotropy in tomographic models, *J. geophys. Res.,* **126**(10), e2021JB022322.

Mainprice, D., 1990. A Fortran program to calculate seismic anisotropy from the lattice preferred orientation of minerals, *Comput. Geosci.,* **16**(3), 385–393.

Mainprice, D., 2007. Seismic anisotropy of the deep earth from a mineral and rock physics perspective, *Treatise Geophys.,* **2,** 437–491.

Mainprice, D., Barruol, G. & Ismaïl, W.B., 2000. The seismic anisotropy of the earth's mantle: from single crystal to polycrystal, *Geophys. Monogr. Ser.,* **117,** 237–264.

Mainprice, D., Tommasi, A., Couvy, H., Cordier, P. & Frost, D.J., 2005. Pressure sensitivity of olivine slip systems and seismic anisotropy of earth's upper mantle, *Nature,* **433**(7027), 731–733.

Mao, Z., Fan, D., Lin, J.-F., Yang, J., Tkachev, S.N., Zhuravlev, K. & Prakapenka, V.B., 2015. Elasticity of single-crystal olivine at high pressures and temperatures, *Earth planet. Sci. Lett.,* **426,** 204–215.

Masalu, D.C., 2007. Mapping absolute migration of global mid-ocean ridges since 80 ma to present, *Earth, Planets Space,* **59**(9), 1061–1066.

Maupin, V., Park, J., Romanowicz, B. & Dziewonski, A., 2007. Theory and observations—wave propagation in anisotropic media, in *Seismology and the Structure of the Earth. Treatise on Geophysics,* Vol. **1,** pp. 289–321, ed. Schubert, G., Elsevier.

McLaughlin, R., 1977. A study of the differential scheme for composite materials, *Int. J. Eng. Sci.,* **15**(4), 237–244.

McNamara, A.K., van Keken, P.E. & Karato, S., 2002. Development of anisotropic structure by solid-state convection in the Earth's lower mantle, *Nature,* **416**(6878), 310–314.

Meade, C., Silver, P.G. & Kaneshima, S., 1995. Laboratory and seismological observations of lower mantle isotropy, *Geophys. Res. Lett.,* **22**(10), 1293–1296.

Molinari, A., Canova, G. & Ahzi, S., 1987. A self consistent approach of the large deformation polycrystal viscoplasticity, *Acta Metall.,* **35**(12), 2983–2994.

Montagner, J.-P. & Kennett, B., 1996. How to reconcile body-wave and normal-mode reference earth models, *Geophys. J. Int.,* **125**(1), 229–248.

Montagner, J.-P. & Nataf, H.-C., 1986. A simple method for inverting the azimuthal anisotropy of surface waves, *J. geophys. Res.,* **91**(B1), 511–520.

Montagner, J.-P., 1998. Where can seismic anisotropy be detected in the earth's mantle? In boundary layers.., *Pure appl. Geophys.,* **151**(2), 223–256.

Montagner, J.-P., Burgos, G., Capdeville, Y., Beucler, E. & Mocquet, A., 2021. The mantle transition zone dynamics as revealed through seismic anisotropy, *Tectonophysics,* **821,** 229133.

Moulik, P. & Ekström, G., 2014. An anisotropic shear velocity model of the earth's mantle using normal modes, body waves, surface waves and long-period waveforms, *Geophys. J. Int.,* **199**(3), 1713–1738.

Moulinec, H. & Suquet, P., 1998. A numerical method for computing the overall response of nonlinear composites with complex microstructure, *Comput. Methods Appl. Mech. Eng.,* **157**(1-2), 69–94.

Nataf, H.-C., Nakanishi, I. & Anderson, D.L., 1984. Anisotropy and shear-velocity heterogeneities in the upper mantle, *Geophys. Res. Lett.,* **11**(2), 109–112.

Nicolas, A. & Christensen, N.I., 1987. Formation of anisotropy in upper mantle peridotites-a review, in *Composition, Structure and Dynamics of the Lithosphere-Asthenosphere System,* Geodynamics Series, Vol. 16, pp. 111–123, eds Fuchs, K. & Froidevaux, C., AGU.

Nowacki, A., 2013. Deformation of the lowermost mantle from seismic anisotropy, in *Plate Deformation from Cradle to Grave: Seismic Anisotropy and Deformation at Mid-Ocean Ridges and in the Lowermost Mantle,* pp. 99–122, Springer.

Núñez-Valdez, M., Wu, Z., Yu, Y. & Wentzcovitch, R., 2013. Thermal elasticity of (Fex,Mg1- x) 2SiO$_4$ olivine and wadsleyite, *Geophys. Res. Lett.,* **40**(2), 290–294.

Núñez-Valdez, M., Da Silveira, P. & Wentzcovitch, R.M., 2011. Influence of iron on the elastic properties of wadsleyite and ringwoodite, *J. geophys. Res.,* **116**(B12), doi:10.1029/2011JB008378.

Ohuchi, T., Fujino, K., Kawazoe, T. & Irifune, T., 2014. Crystallographic preferred orientation of wadsleyite and ringwoodite: effects of phase transformation and water on seismic anisotropy in the mantle transition zone, *Earth planet. Sci. Lett.,* **397,** 133–144.

Ohuchi, T., Kawazoe, T., Nishihara, Y., Nishiyama, N. & Irifune, T., 2011. High pressure and temperature fabric transitions in olivine and variations in upper mantle seismic anisotropy, *Earth planet. Sci. Lett.,* **304**(1-2), 55–63.

Pamato, M.G. *et al.*, 2016. Single crystal elasticity of majoritic garnets: stagnant slabs and thermal anomalies at the base of the transition zone, *Earth planet. Sci. Lett.,* **451,** 114–124.

Panning, M. & Romanowicz, B., 2006. A three-dimensional radially anisotropic model of shear velocity in the whole mantle, *Geophys. J. Int.,* **167**(1), 361–379.

Raterron, P., Chen, J., Geenen, T. & Girard, J., 2011. Pressure effect on forsterite dislocation slip systems: implications for upper-mantle lpo and low viscosity zone, *Phys. Earth planet. Inter.,* **188**(1-2), 26–36.

Raterron, P., Chen, J., Li, L., Weidner, D. & Cordier, P., 2007. Pressure-induced slip-system transition in forsterite: single-crystal rheological properties at mantle pressure and temperature, *Am. Mineral.,* **92**(8-9), 1436–1445.

Raterron, P., Detrez, F., Castelnau, O., Bollinger, C., Cordier, P. & Merkel, S., 2014. Multiscale modeling of upper mantle plasticity: From single-crystal rheology to multiphase aggregate deformation, *Phys. Earth planet. Inter.,* **228,** 232–243.

Raterron, P., Girard, J. & Chen, J., 2012. Activities of olivine slip systems in the upper mantle, *Phys. Earth planet. Inter.,* **200,** 105–112.

Ribe, N.M., 1989. Seismic anisotropy and mantle flow, *J. geophys. Res.,* **94**(B4), 4213–4223.

Ribe, N.M., 1992. On the relation between seismic anisotropy and finite strain, *J. geophys. Res.,* **97**(B6), 8737–8747.

Ricard, Y., Mattern, E. & Matas, J., 2005. Synthetic tomographic images of slabs from mineral physics, in *Earth's Deep Mantle: Structure, Composition, and Evolution,* Geophysical Monograph Series, Vol. **160,** eds Van Der Hilst, R.D., Bass, J.D., Matas, J. & Trampert, J., AGU.

Ringwood, A., 1962. A model for the upper mantle: 2, *J. geophys. Res.,* **67**(11), 4473–4478.

Ringwood, A.E., 1991. Phase transformations and their bearing on the constitution and dynamics of the mantle, *Geochim. Cosmochim. Ac.,* **55**(8), 2083–2110.

Ritterbex, S., Carrez, P. & Cordier, P., 2020. Deformation across the mantle transition zone: a theoretical mineral physics view, *Earth planet. Sci. Lett.,* **547,** 116438.

Saki, M., Thomas, C., Merkel, S. & Wookey, J., 2018. Detecting seismic anisotropy above the 410 km discontinuity using reflection coefficients of underside reflections, *Phys. Earth planet. Inter.,* **274,** 170–183.

Sánchez-Palencia, E., 1980. *Non-Homogeneous Media and Vibration Theory, Lecture Notes in Physics*, Vol. 127, Springer.

Savage, M., 1999. Seismic anisotropy and mantle deformation: what have we learned from shear wave splitting?, *Rev. Geophys.,* **37**(1), 65–106.

Shiraishi, R., Ohtani, E., Kanagawa, K., Shimojuku, A. & Zhao, D., 2008. Crystallographic preferred orientation of Akimotoite and seismic anisotropy of Tonga slab, *Nature,* **455**(7213), 657–660.

Silver, P.G., 1996. Seismic anisotropy beneath the continents: probing the depths of geology, *Annu. Rev. Earth planet. Sci.,* **24,** 385–432.

Simmons, N., Myers, S., Morency, C., Chiang, A. & Knapp, D., 2021. Spiral: a multiresolution global tomography model of seismic wave speeds and radial anisotropy variations in the crust and mantle, *Geophys. J. Int.,* **227**(2), 1366–1391.

Simmons, N.A., Schuberth, B.S., Myers, S.C. & Knapp, D.R., 2019. Resolution and covariance of the LLNL-G3D-JPS global seismic tomography model: applications to travel time uncertainty and tomographic filtering of geodynamic models, *Geophys. J. Int.,* **217**(3), 1543–1557.

Sinogeikin, S.V. & Bass, J.D., 2002. Elasticity of pyrope and majorite–pyrope solid solutions to high temperatures, *Earth planet. Sci. Lett.,* **203**(1), 549–555.

Sinogeikin, S.V., Bass, J.D. & Katsura, T., 2003. Single-crystal elasticity of ringwoodite to high pressures and high temperatures: implications for 520 km seismic discontinuity, *Phys. Earth planet. Inter.,* **136**(1-2), 41–66.

Smyth, J.R., Miyajima, N., Huss, G.R., Hellebrand, E., Rubie, D.C. & Frost, D.J., 2012. Olivine–wadsleyite–pyroxene topotaxy: evidence for coherent nucleation and diffusion-controlled growth at the 410-km discontinuity, *Phys. Earth planet. Inter.,* **200,** 85–91.

Sturgeon, W., Ferreira, A.M., Faccenda, M., Chang, S.-J. & Schardong, L., 2019. On the origin of radial anisotropy near subducted slabs in the midmantle, *Geochem. Geophys. Geosyst.,* **20**(11), 5105–5125.

Thomas, C., Wookey, J., Brodholt, J. & Fieseler, T., 2011. Anisotropy as cause for polarity reversals of d reflections, *Earth planet. Sci. Lett.,* **307**(3-4), 369–376.

Thurel, E. & Cordier, P., 2003. Plastic deformation of wadsleyite: I. High-pressure deformation in compression, *Phys. Chem. Miner.,* **30,** 256–266.

Tielke, J.A., Zimmerman, M.E. & Kohlstedt, D.L., 2016. Direct shear of olivine single crystals, *Earth planet. Sci. Lett.,* **455,** 140–148.

Tommasi, A., Mainprice, D., Canova, G. & Chastel, Y., 2000. Viscoplastic self-consistent and equilibrium-based modeling of olivine lattice preferred orientations: Implications for the upper mantle seismic anisotropy, *J. geophys. Res.,* **105**(B4), 7893–7908.

Tommasi, A., Mainprice, D., Cordier, P., Thoraval, C. & Couvy, H., 2004. Strain-induced seismic anisotropy of wadsleyite polycrystals and flow patterns in the mantle transition zone, *J. geophys. Res.,* **109**(B12), doi:10.1029/2004JB003158.

Tovish, A., Schubert, G. & Luyendyk, B.P., 1978. Mantle flow pressure and the angle of subduction: non-Newtonian corner flows, *J. geophys. Res.,* **83**(B12), 5892–5898.

Vennari, C.E., Lin, F., Kunz, M., Akaogi, M., Miyagi, L. & Williams, Q., 2021. Deformation and strength of mantle relevant garnets: Implications for the subduction of basaltic-rich crust, *Am. Mineral.,* **106**(7), 1045–1052.

Visser, K., Trampert, J., Lebedev, S. & Kennett, B., 2008. Probability of radial anisotropy in the deep mantle, *Earth planet. Sci. Lett.,* **270**(3-4), 241–250.

Wang, N., Montagner, J.-P., Fichtner, A. & Capdeville, Y., 2013. Intrinsic versus extrinsic seismic anisotropy: the radial anisotropy in reference earth models, *Geophys. Res. Lett.,* **40**(16), 4284–4288.

Wang, W., Walter, M.J., Peng, Y., Redfern, S. & Wu, Z., 2019. Constraining olivine abundance and water content of the mantle at the 410-km discontinuity from the elasticity of olivine and wadsleyite, *Earth planet. Sci. Lett.,* **519,** 1–11.

Weidner, E., Beghein, C., Huang, Q. & Schmerr, N., 2022. Upper mantle radial anisotropy under the Indian ocean from higher mode surface waves and a hierarchical transdismensional approach, *Geophys. J. Int.,* **228**(1), 78–101.

Wookey, J. & Kendall, J.-M., 2004. Evidence of midmantle anisotropy from shear wave splitting and the influence of shear-coupled P waves, *J. geophys. Res.,* **109**(B7), doi:10.1029/2003JB002871.

Yuan, K. & Beghein, C., 2013. Seismic anisotropy changes across upper mantle phase transitions, *Earth planet. Sci. Lett.,* **374,** 132–144.

Zhang, S. & Karato, S.-i., 1995. Lattice preferred orientation of olivine aggregates deformed in simple shear, *Nature,* **375**(6534), 774–777.

Zhou, W.-Y., Hao, M., Zhang, J.S., Chen, B., Wang, R. & Schmandt, B., 2022. Constraining composition and temperature variations in the mantle transition zone, *Nat. Commun.,* **13**(1), 1–9.